Journal of Photochemistry & Photobiology, A: Chemistry 459 (2025) 116056

Contents lists available at ScienceDirect

Journal of Photochemistry & Photobiology, A: Chemistry

journal homepage: www.elsevier.com/locate/jphotochem

Enhanced super-ultra-deep photocatalytic oxidative desulfurization by titanium-activated metal-organic frameworks nanophotocataltyst

Mehdi Beshtar [a], Afsanehsadat Larimi [b,*], Ali Akbar Asgharinezhad [c,*]

[a] Department of Chemical and Petroleum Engineering, Sharif University of Technology, Tehran, Iran
[b] School of Engineering and Applied Sciences, Department of Chemical Engineering, Swansea University, Wales, UK
[c] Chemistry and Process Research Department, Niroo Research Institute, Tehran, Iran

ARTICLE INFO

Keywords:
Titanium
MIL-101(Fe)
Dibenzothiophene
Pseudo-first-order kinetic model
Photocatalytic oxidative desulfurization
Hydrogen peroxide

ABSTRACT

Addressing the escalating global demand for fossil fuels and the urgent environmental concerns associated with their use necessitates the development and implementation of efficient and cost-effective techniques for the removal of sulfur compounds. In this study, titanium-activated MIL-101(Fe) was utilized for the removal of organosulfur compounds through the photocatalytic oxidation desulfurization (PODS) process. The coexistence of active sites with titanium and iron resulted in an ultra-deep desulfurization. The impact of titanium loading was assessed, with TxML representing the ratio of Ti to Fe (x = 1, 1.5, and 2, respectively). Nanophotocatalysts were fabricated by solvothermal method. The physicochemical properties of the new materials were investigated by performing XRD, TEM, FT-IR, FESEM, EDX, UV–Vis DRS, PL, GC–MS, ESR, TGA, transient photocurrent, and nitrogen adsorption–desorption analyses. The effect of titanium loading on the structure, and performance of photocatalysts in the PODS reaction was investigated. The reaction parameters were optimized for maximum efficiency. Under optimal conditions of T2ML loading at 1.5 g/L, a volumetric solvent to fuel ratio (S/F) of 1, and a temperature of 50 ℃, T2ML shows the best performance by removing 100 % of dibenzothiophene.

Kinetic experiments revealed that the PODS reaction obeys a pseudo-first order equation, and activation energy is 47.08 kJ.mol^{-1}.

1. Introduction

In recent decades, the global demand for fossil fuels, particularly petroleum derivatives, has experienced a significant upsurge. Several key factors contribute to this increased demand, which including population growth, the advancement of transportation infrastructure, and the expansion of various industrial sectors [1].

The presence of sulfur compounds, including mercaptans, sulfides, disulfides, thiophene, benzothiophene, and dibenzothiophene, in fossil fuels poses significant challenges in various industrial settings. These compounds contribute to multiple issues, such as the corrosion of industrial equipment, deactivation of fuel cell electrodes and catalytic converters, and damage to car engines. Therefore, it is crucial to develop and implement effective desulfurization methods to minimize the detrimental effects of these sulfur compounds in fossil fuels, ultimately ensuring the efficient, safe, and sustainable operation of industrial processes and equipment [2].

Additionally, the combustion of fossil fuels containing sulfur compounds leads to the release of sulfur oxides (SOx, x = 2, 3), which have been recognized as a major contributor to acid rain. Acid rain has been associated with several detrimental environmental and human health effects. These harmful consequences emphasize the importance of mitigating SOx emissions through the implementation of advanced technologies and strategies to protect the environment and promote public health [3].

Hydrodesulfurization (HDS) is the conventional industrial method for sulfur compound degradation in numerous industries, including petrochemicals and refineries. In addition to the challenging operating conditions (pressure > 2500 kPa, temperature = 300–500 °C), the removal of cyclic sulfur compounds like thiophene (Th), 4,6-dimethyl dibenzothiophene (4,6-DMDBT), benzothiophene (BT), and dibenzothiophene (DBT) remains limited in the HDS process [4]. The development of an advanced sulfur removal processes is of paramount importance to achieve deep desulfurization. Extractive desulfurization (EDS), adsorptive desulfurization (ADS), oxidative desulfurization (ODS), photocatalytic oxidative desulfurization (PODS), and oxidation-

* Corresponding authors.
E-mail addresses: a.larimi@swansea.ac.uk (A. Larimi), aasgharinezhad@nri.ac.ir (A.A. Asgharinezhad).

https://doi.org/10.1016/j.jphotochem.2024.116056
Received 1 July 2024; Received in revised form 21 August 2024; Accepted 28 September 2024
Available online 30 September 2024

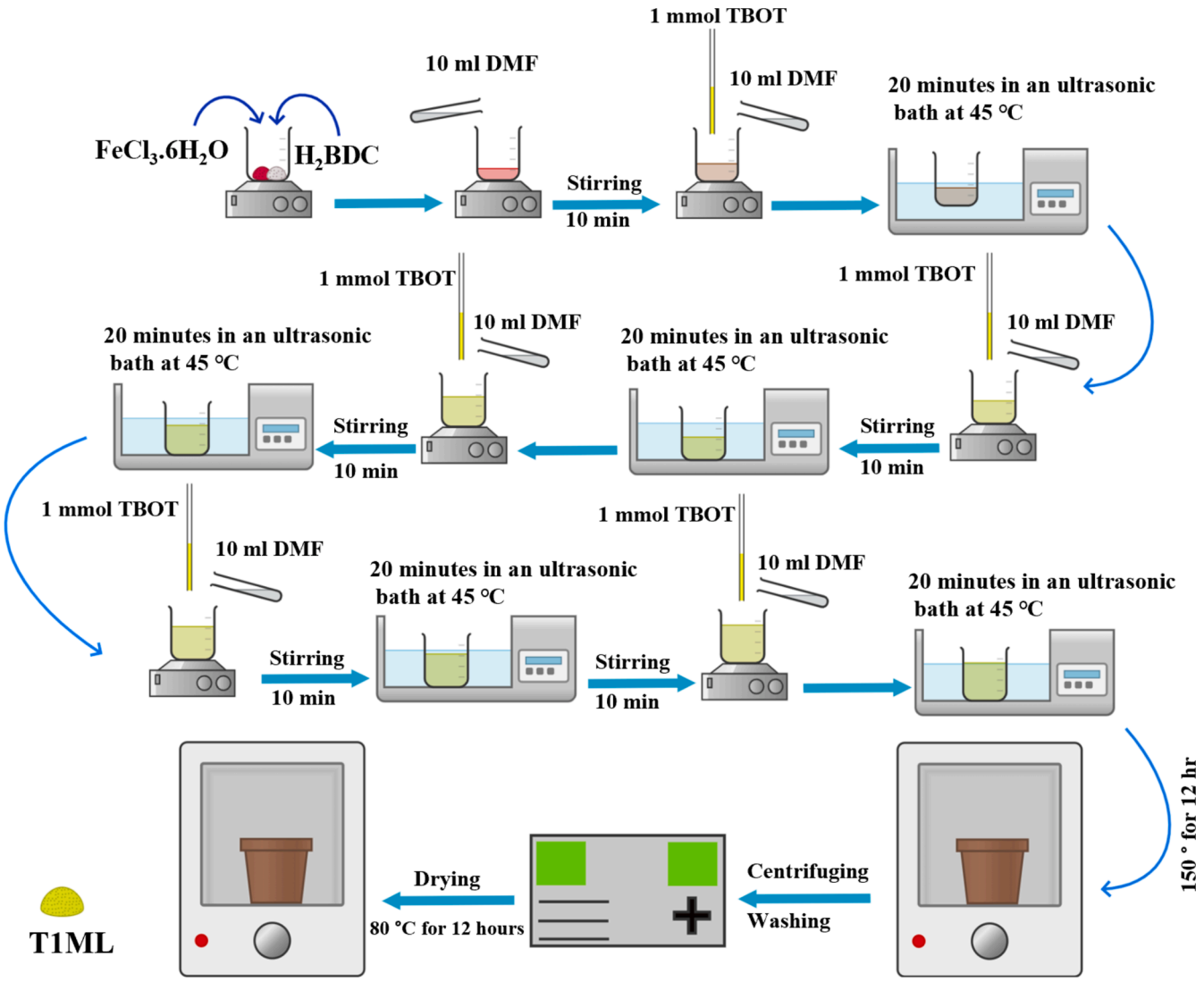

Fig. 1. Schematic of T1ML synthesis steps.

extraction desulfurization (OEDS) have been studied as alternatives or complements to the HDS process [5], and the PODS method has received much attention owing to its mild operating conditions (ambient pressure, temperature < 100 ℃) and low cost [6]. In general, the PODS reaction involves the oxidation of S-containing materials to sulfones and polarized sulfoxides by means of appropriate light irradiation and the action of catalyst sites, which are then separated by a polar solvent, resulting in the production of a clean fuel [7].

Porous materials composed of organic ligands and inorganic clusters, called metal–organic frameworks (MOFs), possess promising properties such as low density, high mechanical stability, high specific surface area, uniform pore structure, tunable porosity, and high thermal stability [8,9]. These materials have recently been used in various fields such as catalysis [10], drug delivery [11], storage [12], membranes [13], photocatalysis [14], and separation [15]. In recent years, the use and development of clustered Fe MOFs as heterogeneous catalysts have garnered great interest due to their high stability toward oxidizing agents and water [16], usability in a wide range of pH values [17], and the broad and uniform distribution of iron as a catalyst [18]. MIL-101 (Fe) (MIL is the abbreviation of the Material Institute Lavoisier) is an iron-based MOF composed of 1,4-benzenedicarboxylic acid linkers and octahedral chains of Fe(III) as secondary building units (SBUs). Features such as functional linkers, adjustable pores, and surface properties have attracted the attention of many researchers to MIL-101(Fe) [19].

One of the primary challenges is the high cost of synthesizing MOFs on a large scale, prompting researchers to focus on the simplest activation methods for these materials in different fields. Active species like Mo [20], Ni [21], Mn and Cu [22] have significantly increased the activity of MOFs in various reactions. The high cost of using MOFs as catalysts is a concern; thus, our research has sought to reduce expenses by employing a straightforward synthesis method. Moreover, the photocatalyst's efficiency remains unaltered, and deep desulfurization is achieved through the introduction of a novel and uncomplicated structure. To decrease the economic costs associated with MOF synthesis (easy synthesis) for large-scale industrial use, it was imperative to identify a suitable catalyst base. MIL-101(Fe) was selected due to its availability, high specific surface area, and adaptability for large-scale synthesis. Titanium was chosen as the active component because of its accessibility and proven efficacy as both a catalyst and a photocatalyst.

In this study, we successfully loaded varying amounts of active Ti species onto the MIL-101(Fe) structure using a solvothermal synthesis method. Compared to other methods aimed at advancing the PODS reaction [23,24], this innovative approach has demonstrated a substantial improvement in the overall performance of MOFs and photocatalysts, contributing to the ongoing quest for more efficient and sustainable catalytic materials. The resulting materials were evaluated for their physicochemical properties, with a specific focus on their photocatalytic performance under visible light irradiation. By introducing Ti species

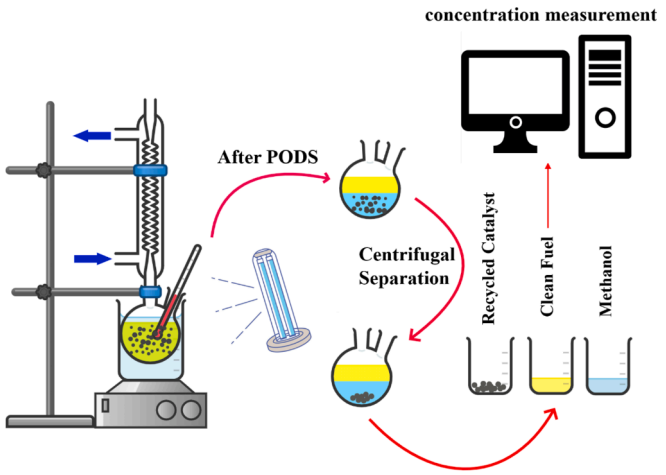

Fig. 2. Schematic of photocatalytic system.

onto the MIL-101(Fe) structure, we aimed to enhance the material's photocatalytic activity and efficiency, leveraging the unique properties of the MIL-101(Fe) framework.

2. Materials and method

2.1. Materials

The purity percentage of commercial reagents utilized in the synthesis of photocatalysts remained unchanged. These included terephthalic acid (H_2BDC, ≥98 %, Merck), Iron(III) chloride hexahydrate ($Cl_3FeH_{12}O_6$, ≥99 %, Merck), *N, N*-dimethylformamide (DMF, ≥99.5 %, Merck), and tetra-n-butyl orthotitanate (TBOT, ≥98 %, Merck). The following solvents were used: acetonitrile (CHN, ≥99 %, Merck), ethanol (EtOH, 96 %, Merck), n-octane (≥99 %, Merck), and methanol (≥995 %, Merck). The following reagents were used: 4,6-dimethyldibenzothiophene (4,6-DMDBT, ≥98 %, Merck), dibenzothiophene (DBT, ≥98 %, Merck), benzothiophene (BT, ≥98 %, Merck), and hydrogen peroxide (H_2O_2, 30 %, Merck).

2.2. Synthesis of MIL-101(Fe)

A synthesis of MIL-101(Fe) was carried out through a solvothermal method adapted from previously reported procedures [25], with certain modifications incorporated. The procedure involved dissolving 2.7 g (10 mmol) of Iron(III) chloride hexahydrate and 0.83 g (5 mmol) of terephthalic acid in 60 ml of DMF. To obtain a homogeneous solution, the resultant mixture was subjected to ultrasonic treatment at ambient temperature for a duration of 20 min. Subsequently, the solution was solvothermally processed in a stainless steel autoclave at 110 °C overnight. Upon cooling to room temperature, the mixture was centrifuged and washed with DMF and hot ethanol (50 °C) for three cycles. The resultant product was isolated and dried at 80 °C for a 12-hour period.

2.3. Synthesis of Ti-MIL-101(Fe)

The synthesis of T1MIL was conducted through a multi-step process involving the combination of Iron(III) chloride hexahydrate, terephthalic acid, and TBOT in a controlled manner. Initially, 1.35 g (5 mmol) of ferric chloride hexahydrate and 0.415 g (2.5 mmol) of terephthalic acid were dissolved in 10 ml of DMF and mixed vigorously for ten minutes using a mechanical stirrer at ambient temperature. Subsequently, 5 mmol (1.7 gr) of TBOT was added to the mixture in five steps, with 1 mmol added in each step, and 10 ml of DMF was simultaneously added during each step. Following each step, the resulting mixture was stirred for ten minutes to ensure a homogeneous solution, which was then placed in an ultrasonic bath at 45 °C for twenty minutes. ultimately, the resulting solution was transferred to an autoclave and heated in an oven at 150 °C overnight. The synthesized mixture was subsequently separated and dried according to the procedures described in section 2.2 and designated as TxML (where x represents the Ti/Fe molar ratio, with Ti/Fe = 1, 1.5, and 2). The synthesis steps of T1ML are further illustrated in Fig. 1.

2.4. Characterization assay

A Bruker D8 device was employed to collect X-ray diffraction patterns (XRD) of the synthesized samples using Cu Kα radiation at 30 mA and 40 kV. In order to investigate the chemical bonds and functional groups formed, the Fourier transform infrared (FTIR) spectrum of the synthesized samples was analyzed using a Bruker Equinox spectrometer (500–4000 nm). Energy dispersive X-ray spectroscopy (EDX) and field emission scanning electron microscopy (FESEM) were performed using a TESCAN MIRA at a voltage of 15 kV in order to detect the morphologies and microstructures of the materials. The Shimadzu UV-2700 device was employed to collect the UV–Vis diffuse reflectance spectroscopy (DRS) spectra of the synthesized photocatalysts. These data were then utilized to compute the bandgap of the samples. Morphological properties of the synthesized material were evaluated via transmission electron microscopy (TEM) analysis, conducted using the Philips EM 208S operating at 100 kV. ASAP 2020, Micromeritics (USA) was employed to obtain specific characteristics using Brunauer–Emmett–Teller (BET) method. In order to explore the rate of recombination of electrons and holes during the photocatalytic process, the photoluminescence (PL) spectrum of the fabricated materials was obtained using a G9800A fluorescence spectrophotometer. The time-resolved photoluminescence (TRPL) spectra of the synthesized samples were obtained using the Shimadzu RF-6000 to assess the recombination rate of charge carriers in photocatalysts. The Shimadzu PDA-7000 was employed to ascertain the transient photocurrent of the synthesized samples. The thermal stability of the optimal sample was also evaluated using thermogravimetric analysis (TGA) in the range of 50–800 °C (heating rate, 5 °C/min). The present study aimed to investigate the stability and quantity of photogenerated radicals produced during the photocatalytic process. To this end, 5,5-Dimethyl-1-pyrroline N-oxide (DMPO) was employed as a spin-trapping agent, in conjunction with the JEOL FA-300 instrument. UV–Vis absorption spectra were obtained using a Shimadzu UV-160A spectrophotometer in the wavelength range of 200–700 nm. The quantity of sulfur compounds in each stage of the process was quantified at a wavelength of 325 nm [26]. To ascertain the nature of the reaction product, gas chromatography-mass spectrometry (GC–MS) analysis was conducted using the Shimadzu GC–MS QP 2010 device. The results of the electrochemical impedance spectroscopy (EIS) tests were obtained in the frequency range of 10^{-6}–10^{-2} Hz and with an amplitude of 4 mV in the electrochemistry laboratory.

2.5. PODS process

The photocatalytic system was composed of a two-neck flask, a condenser, a mechanical stirrer, a water stirrer, and a 250 W sodium vapor lamp. PODS activity was evaluated on model fuel (*n*-octane) with concentrations of 250, 500, 1000, 2000, 4000, and 5000 ppm DBT. Catalyst activity was also evaluated for the removal of BT, Th and 4,6-DMDBT, sulfur compounds at a concentration of 250 ppm. The two-phase reaction mixture, which consisted of 30 ml of methanol as the solvent, 30 ml of model fuel, and 0.075 g of catalyst, underwent vigorous stirring for 45 min in a dark condition to reach an adsorption equilibrium state. In the following step, 10 μl of 30 wt% H_2O_2 was introduced into the reaction solution. Subsequently, the lamp was activated to initiate the photocatalytic oxidation reaction which ran for an additional 75 min. The samples taken from the reaction media were immediately centrifuged (6000 rpm, 10 min) and diluted with 3 ml of pure *n*-octane.

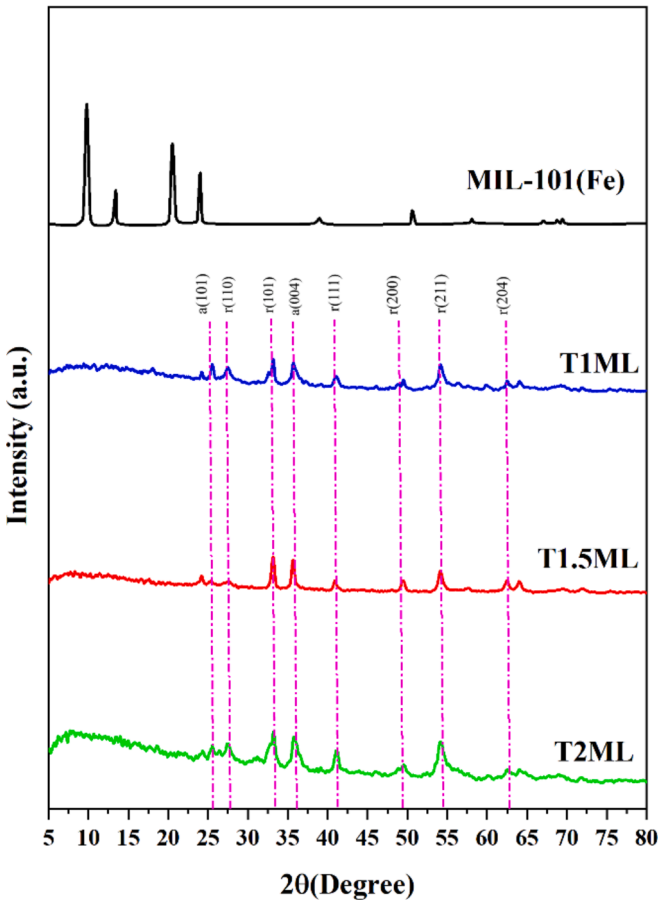

Fig. 3. XRD patterns of synthesized materials, r(rutile), a(anatase) (The data has been subjected to a five-degree smoothing process.).

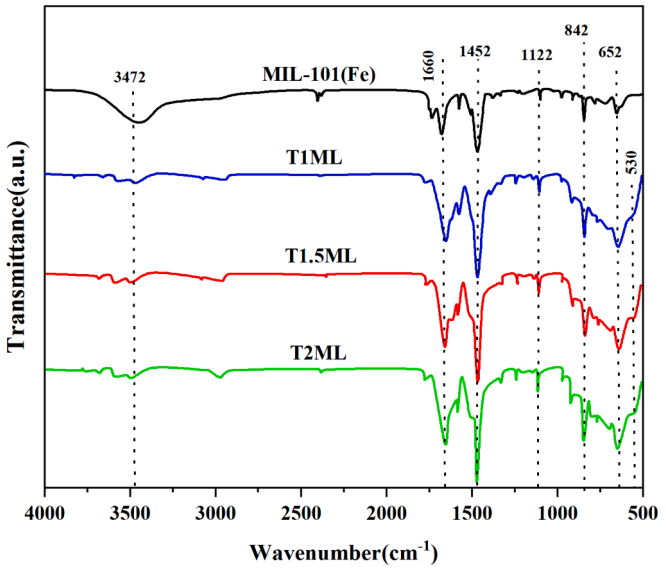

Fig. 4. FTIR spectra of synthesized materials (The data has been subjected to a five-degree smoothing process).

The removal% and organosulfur content were determined using equation 1 and the schematic of the photocatalytic system is demonstrated in Fig. 2.

$$\text{Sulfur compound Removal } (\%) = \frac{C_0 - C_t}{C_0} \times 100 \quad (1)$$

The concentration of sulfur compounds before performing the process (t = 0), designated as C_0, and at t min, designated as C_t, are represented by the variables C_0 and Ct, respectively.

3. Results and discussion

3.1. Characterization assay

At first, the structure of the synthesized samples was explored by XRD, as shown in Fig. 3. The XRD pattern acquired for MIL-101(Fe) resembles previous findings [27,28]. It exhibited well-defined peaks at 5°, 10°, and 15°, which suggests that MIL-101(Fe) was synthesized accurately. The XRD pattern obtained from TxML photocatalysts are comparable to each other, but distinct from the MIL-101(Fe) pattern. This observation suggests that titanium loading onto the MIL-101(Fe) framework has altered the MOF network structure. The obtained patterns for TxML photocatalysts suggests the generation of anatase (a) and rutile (r) titanium dioxide. The detected peaks at 2θ of 25.5, 27.6, 33.3, 35.9, 41.2, 48.9, 54.2, and 62.9 correspond to the characteristic planes of a(101), r(110), r(101), a(004), r(111), r(200), r(211), and r(204), respectively (ICDD 00-021-1272 and 00-21-1276) [29,30]. Fig. 3 indicates that with increasing titanium loading, peak intensity noticeably increases, indicating a greater likelihood of forming titanium dioxide. Additionally, the XRD analysis yielded clear evidence that titanium loading has resulted in a substantial alteration of the MOF network, even leading to its destruction. Consequently, the MOF peaks at 2θ = 5°, 10°, and 15° in the structure of the photocatalysts TxML were not identified. This suggests that the synthesized samples are composite and possess a heterojunction structure.

To determine the functional groups of the fabricated materials, their FTIR spectra were evaluated as shown in Fig. 4. For all spectra, the bands observed at 1660 and 1530 cm^{-1} are related to the asymmetric stretching of carboxyl groups [31,32]. The weak absorption at 1122 cm^{-1} indicates the C-H bending of H_2BDC [33]. The broad band at 3472 cm^{-1} illustrates the O-H vibratory stretching in the H_2BDC [34]. The diminished intensity of the peak at 3472 cm^{-1} in the TxML samples relative to MIL-101(Fe) can be ascribed to the diminished quantity of H_2BDC utilized in the synthesis of the TxML photocatalysts. The peak at approximately 842 cm^{-1} is associated with the C-H vibration in H_2BDC, while the peaks at 652 cm^{-1} are attributed to the μ_3-O stretching [35]. The absorption peak at 1452 cm^{-1} is corresponded to the OCO asymmetric stretching carboxylate group in the H_2BDC. The Ti-O stretching band, attributed to the 530 cm^{-1} band, is exclusively observed in TxML photocatalysts containing titanium [36]. The FTIR results affirm the effective fabrication of MIL-101(Fe), with the successful loading and introduction of titanium.

To investigate the morphology of the synthesized materials, FESEM and TEM techniques were employed, as illustrated in Figs. 5 and 6. The synthesis of MIL-101(Fe) was found to be successful based on the findings in Fig. 5(a and b). The FESEM images obtained from TxML photocatalysts (Fig. 5(c-f)) demonstrate that the loading of titanium into the MOF structure has resulted in notable alterations to the network and the dimensions of its crystals. These changes include an increase in crystal size and the emergence of a highly uneven surface, findings that align with those observed in the XRD analysis. As illustrated in Fig. 6, the TEM images reveal that the dimensions of the crystals relative to the MOF have undergone a significant alteration in the T1.5ML and T2ML samples. This is attributed to the increased loading of titanium, which has resulted in a notable change in the crystal structure. Additionally, the surfaces of T1.5ML and T2ML exhibit a noticeable roughness, particularly at the edges of the crystals. This observation is indicative of a distinct change in the crystal morphology. The examination of the T1ML sample's mapping images (Fig. 7) reveals a homogeneous dispersion of

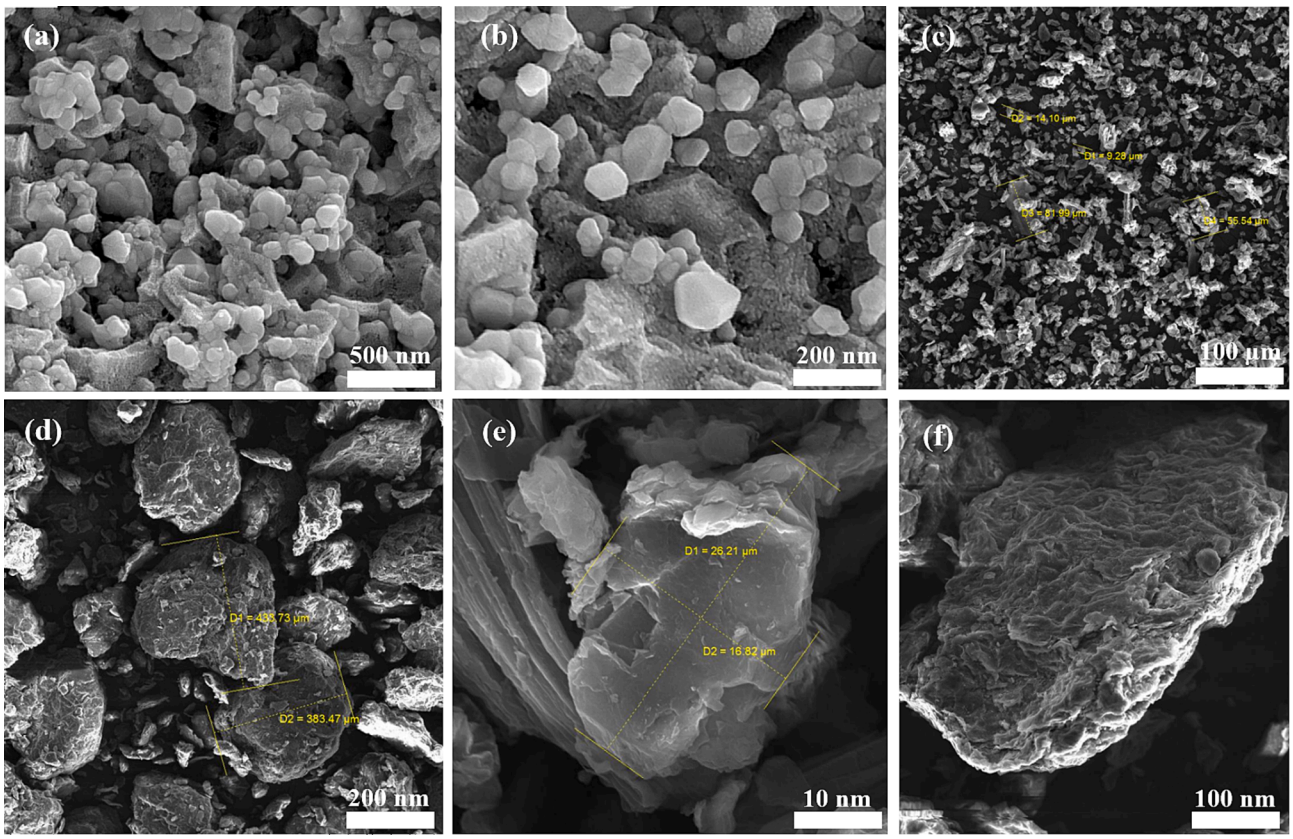

Fig. 5. FESEM micrographs of prepared samples: (a),(b) MIL-101(Fe), (c), (d) T1.5ML, (e), (f) T2ML.

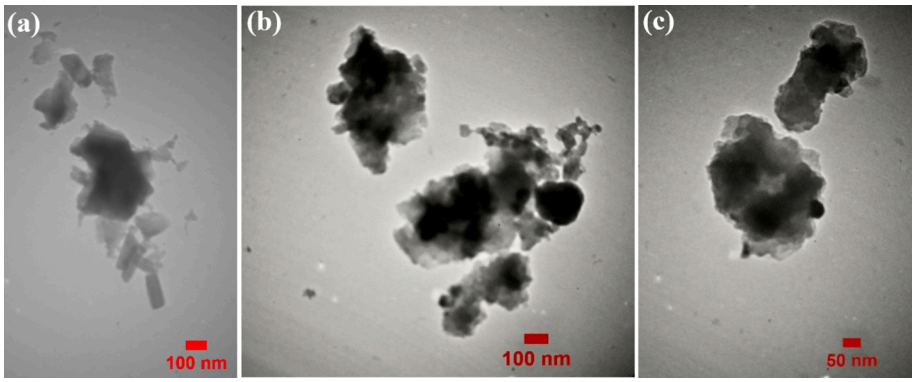

Fig. 6. TEM micrographs of synthesized materials: (a) MIL-101(Fe), (b) T1.5ML, (c) T2ML.

Fe, while Ti exhibits a more heterogeneous distribution. This observation suggests that the employed synthesis method successfully utilized the MOF as a support structure for active titanium species. Ultimately, the formation of TxML composites can be attributed to the deposition of titanium particles on the MOF's surface, as evidenced by the observed differences in elemental distribution.

Results of the N_2-physisorption experiments are demonstrated in Fig. 8(a). The findings indicate that the specific surface area decreases with the growing introduction and loading of titanium. This is attributed to the blockage of the holes by titanium and the consequent reduction of nitrogen adsorption. The results from BJH (Fig. 8(b)) demonstrate that an increase in titanium loading is associated with a reduction in both pore volume and diameter. The sharp decrease in the specific surface area of T2ML, as indicated by BET analysis, suggests that the T2ML sample contains a greater number of titanium active sites than other synthesized materials. This is consistent with the hypothesis that these sites facilitate the reaction and contribute to the observed high reactivity. This outcome aligns with the results gathered from BET analysis (Table 1). A comparison of the results of XRD, FESEM, and BET analysis reveals that the synthesized samples exhibit a composite structure, wherein titanium serves as the primary active component of the reaction and MIL-101(Fe) functions as a support.

Turnover frequency (TOF) is a measure of the specific activity of catalytic centers of the TxML nanophotocatalysts, defined as the number of molecular reactions or catalytic cycles occurring at the center per unit of time. TOF for TxML nanophotocatalysts enables a high number of catalytic cycles to be completed per unit time. The TOF is calculated using the following equation [37], the value of which is reported for each of the synthesized materials in Table 1.

$$\text{TOF} = \frac{\text{Mole number of DBT converted}}{(\text{Mole of active site specise in the nanophotocatalyst}) \times (\text{reaction time})} \quad (2)$$

The study of the PL spectra of the new materials was conducted to investigate the recombination rate of photogenerated h^+ and e^- [38], illustrated in Fig. 9(a). The spectra within the range of 340–350 nm display a broad peak, as depicted in Fig. 9(a), this peak results from the recombination of h^+ and e^- between the valence and conduction bands. Generally, as the PL intensity decrease, the recombination rate of e^- and holes h^+ decreases [39]. Additionally, the stability of the photocatalyst decreases, resulting in decreased performance in the PODS reaction.

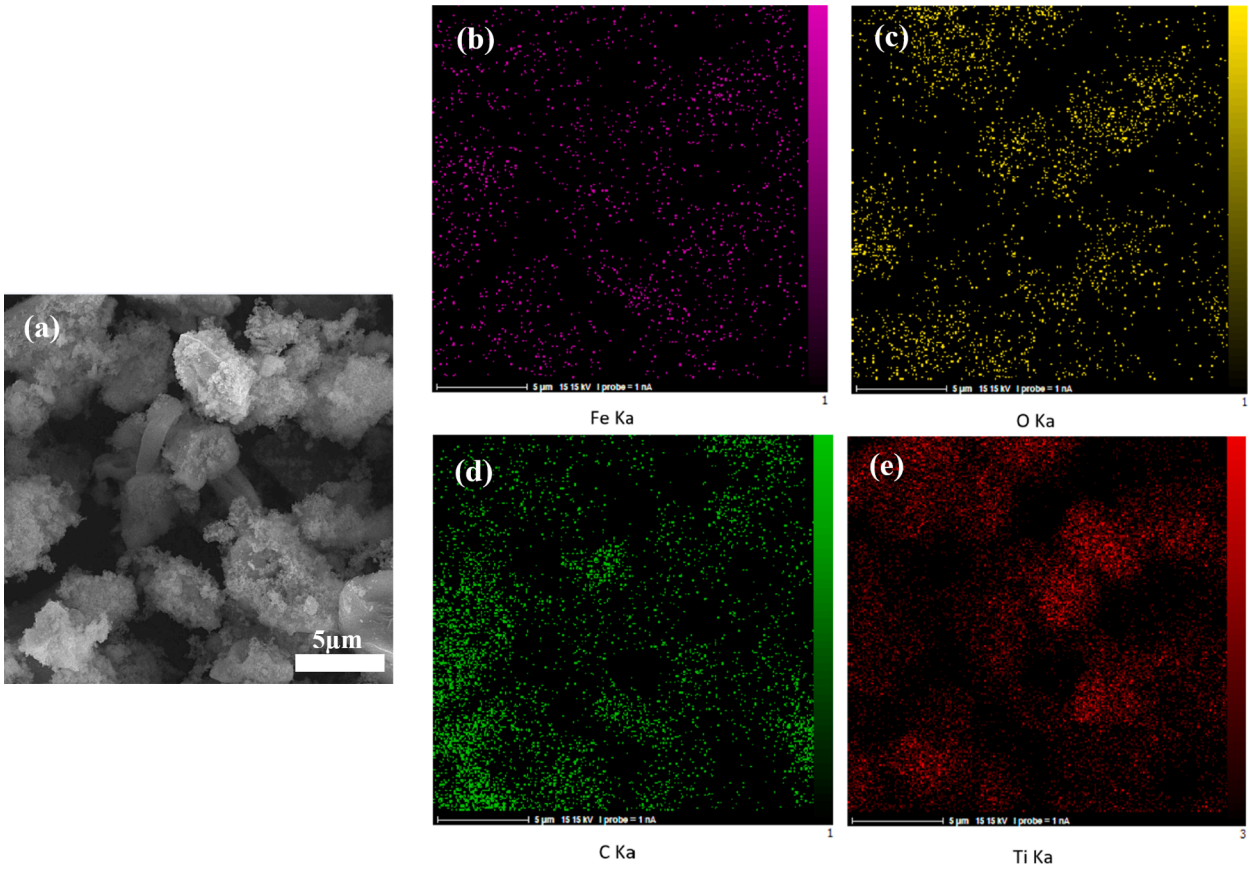

Fig. 7. FESEM and EDX mapping images of T1ML.

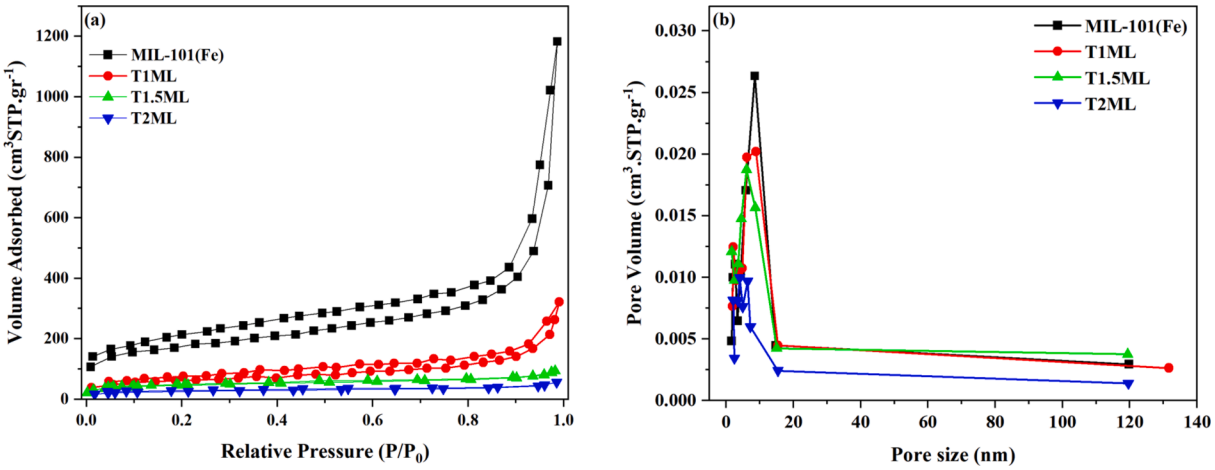

Fig. 8. (a) BET analysis and (b) BJH pore size distributions of prepared photocatalysts.

Table 1
The surface characteristics along with band-gap energy of the prepared materials.

Photocatalyst	S_{BET} (m^2/g)	Pore Volume (cm^3/g)	Band-gap (eV)	Pore diameter (nm)	TOF (min^{-1})
MIL-101(Fe)	541.3	1.6531	2.94	3.5711	7.451
T1ML	184.51	0.9457	2.60	3.3167	7.022
T1.5ML	106.79	0.6159	2.51	2.31455	6.340
T2ML	82.23	0.4166	2.25	2.2534	5.212

Fig. 9(a) illustrates that an increase in titanium loading results in a reduction in the PL intensity. This is due to the fact that an increase in the titanium loading leads to changes and degradation of the structure of the synthesized photocatalysts, creating additional pathways for the migration of h^+ and e^- to the valence and conduction bonds. Consequently, the lifetime and stability of the excited e^- and h^+ are enhanced [40]. Based on its low PL spectra intensity, T2ML is anticipated to exhibit superior photocatalytic performance.

In order to explore the behavior of charge carriers excited by light radiation [41], a TRPL analysis was conducted, the results of which are presented in Fig. 9(b). The findings indicate that an increase in the

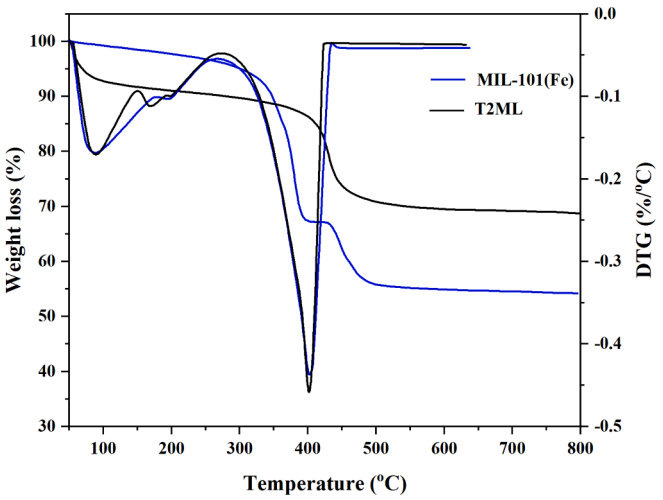

Fig. 11. TGA/DTG curve of MIL-101(Fe) and (T2ML).

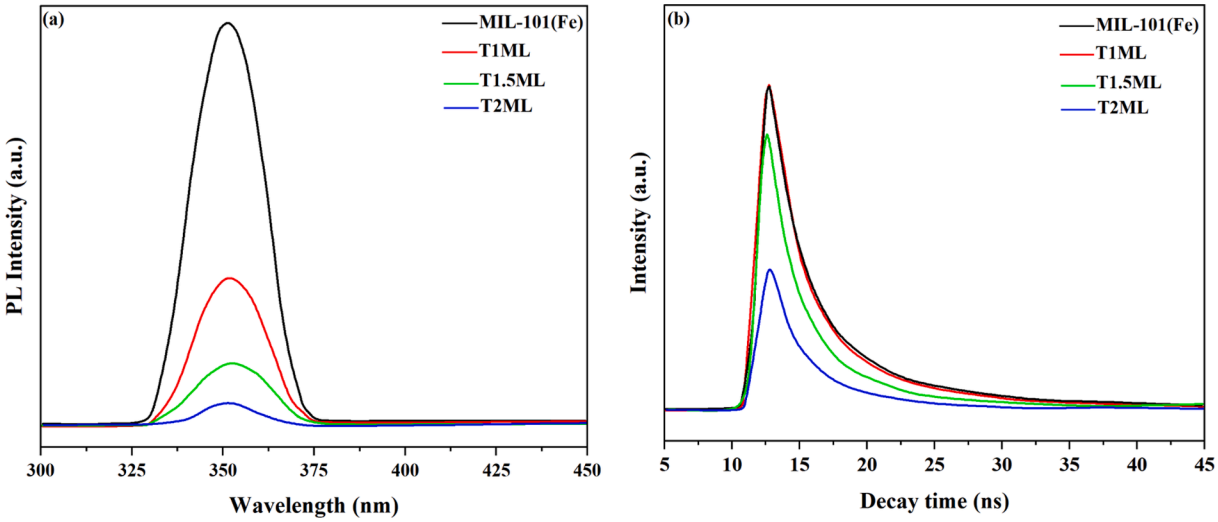

Fig. 9. PL spectra (a) and TRPL spectra (b) of synthesized photocatalysts (The data has been subjected to a five-degree smoothing process).

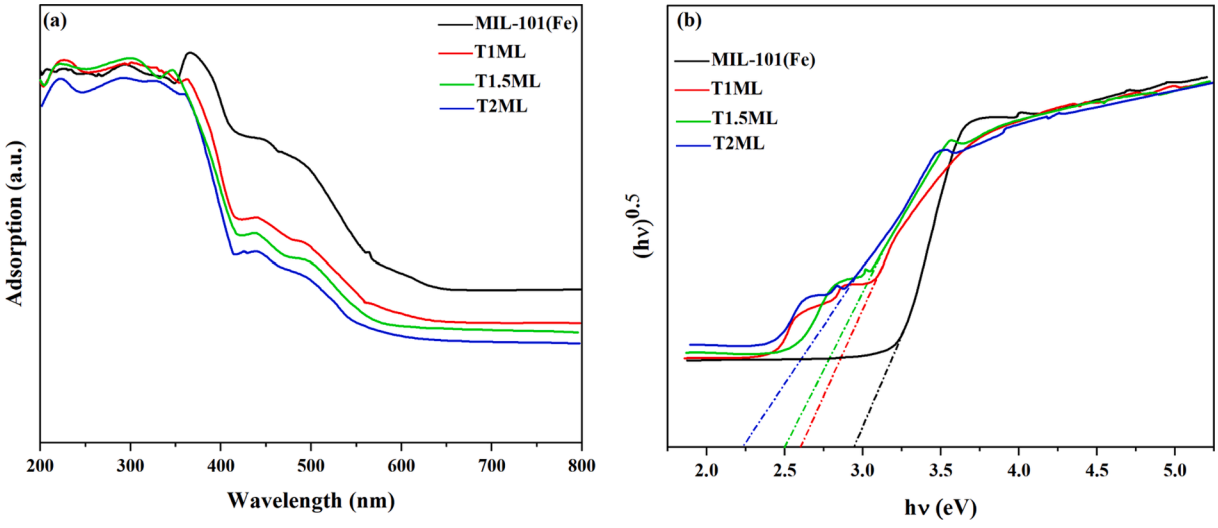

Fig. 10. (a) DRS spectra of the photocatalysts and (b) Tauc plot to calculate bandgap energies. (The data has been subjected to a five-degree smoothing process).

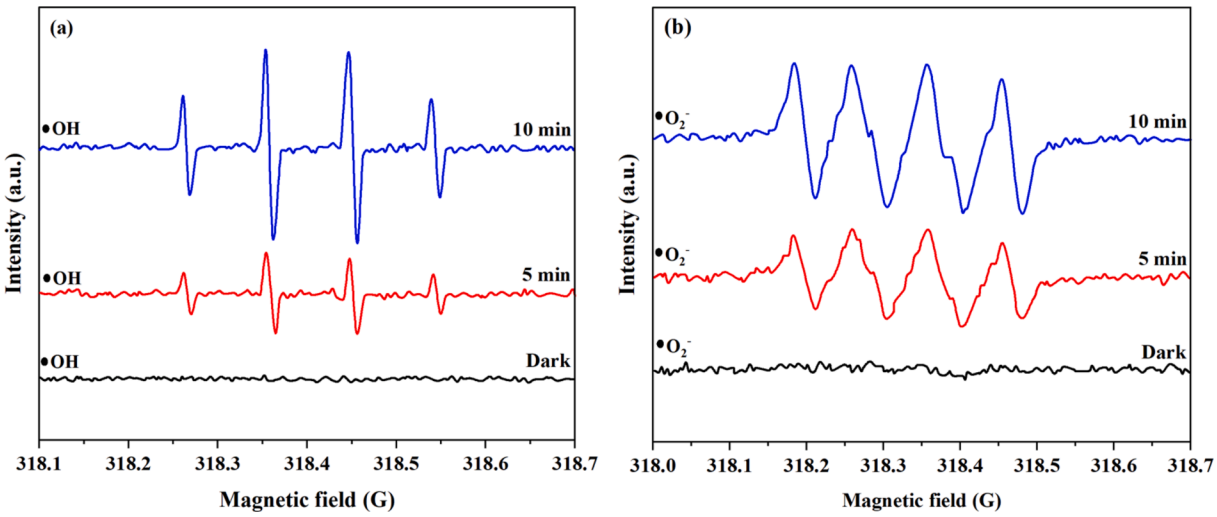

Fig. 12. The ESR spectrum of DMPO-·O_2 and DMPO-·OH were obtained under dark conditions and in the presence of visible light irradiation.

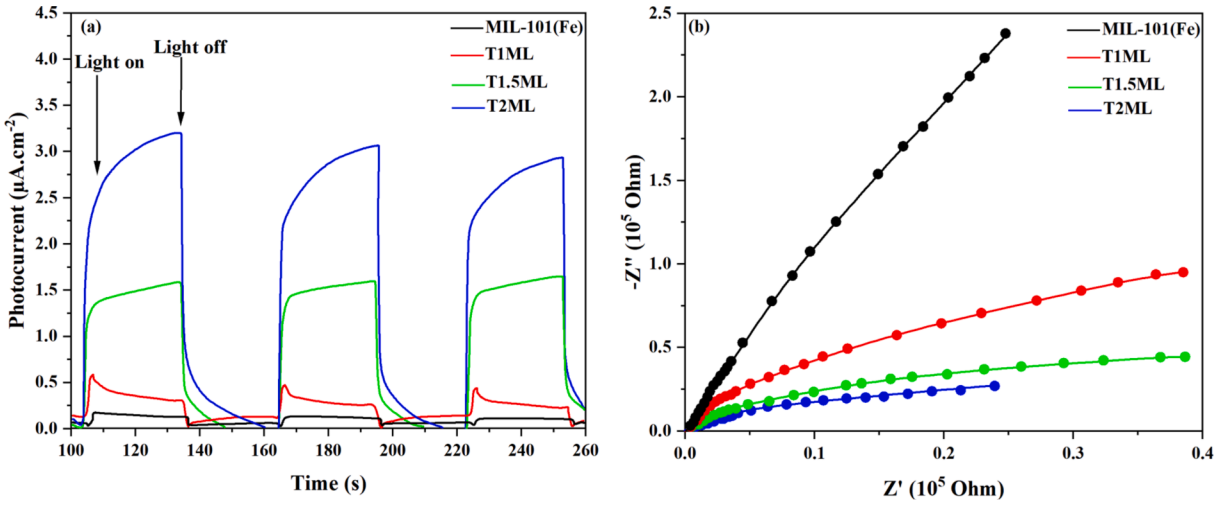

Fig. 13. Transient photocurrent (a) and Nyquist diagrams (b) of synthesized materials.

quantity of titanium loading results in a reduction in the recombination rate of charge carriers stimulated by light [42]. The obtained spectra indicate that T2ML can act as an efficient electron acceptor during the PODS reaction, which leads to an increase in photocatalytic activity and ultimately to an increase in the production of •OH and $•O_2^-$ radicals due to the reduction. The recombination rate of charge carriers is directly related to the increase in the production of •OH and $•O_2^-$ radicals.

The utilization of sunlight and visible light plays a crucial role in the formulation and construction of photocatalysts [43]. One crucial stage of photocatalytic reactions involves light photon absorption. Accordingly, the optical properties of the synthesized materials were appraised via the DRS technique, which is illustrated in Fig. 10(a). In all the samples, there is a notable decline in the absorption of wavelengths below 400 nm, which raleted to the band gap energy of synthesized materials. The optical absorption of the synthesized samples was found to correlate with their bandgap. The Kubelka-Munk equation and the associated Tauc plots were employed to determine the bandgap of the synthesized materials [44]. This correlation is shown in Fig. 9(b). As shown in Fig. 10(b), it is apparent that the gap band diminishes with higher levels of titanium loading. This phenomenon can be attributed to both the alteration of the samples' crystal phase and the structural damage incurred [45]. The synthesized materials' bandgap is shown in Table 1.

The thermal stability of MIL-101(Fe) and T2ML was evaluated through TGA/DTG within the temperature range of 0–800 °C, as displayed in Fig. 11. TGA curves indicate that MIL-101(Fe) and T2ML are highly stable up to 300 °C, rendering them appropriate for PODS reaction to eliminate organosulfur compounds. The loss of weight, up to 300 °C, can be attributed to the evaporation of surface moisture, trapped water, and DMF molecules within the photocatalyst structure [46]. At temperatures ranging from 350 to 500 degrees Celsius, the photocatalyst undergoes hydroxylation [47]. Complete destruction of the photocatalyst occurs at 550 °C. T2ML exhibited greater thermal stability compared to MIL-101 (Fe), experiencing a weight loss of 28 % up to a temperature of 500 °C.

The ESR spectra of the T2ML are shown in Fig. 12. The DMPO-·OH and DMPO-·O_2^- have been identified, indicating the formation of these radicals in the presence of visible light. Fig. 12(a) and 12(b) display the intensity of the generated ·OH and ·O_2^- radicals in the absence of light and under visible light exposure, respectively. Hydroxy and superoxide radicals are minimally generated under low light conditions and the ESR spectra exhibit low levels of intensity. The intensity of the radicals produced exhibited an upward trend with time, indicative of the outstanding photocatalytic performance of T2ML.

The transient photocurrent of the fresh samples was obtained under visible light irradiation, as illustrated in Fig. 13(a). According to Fig. 13

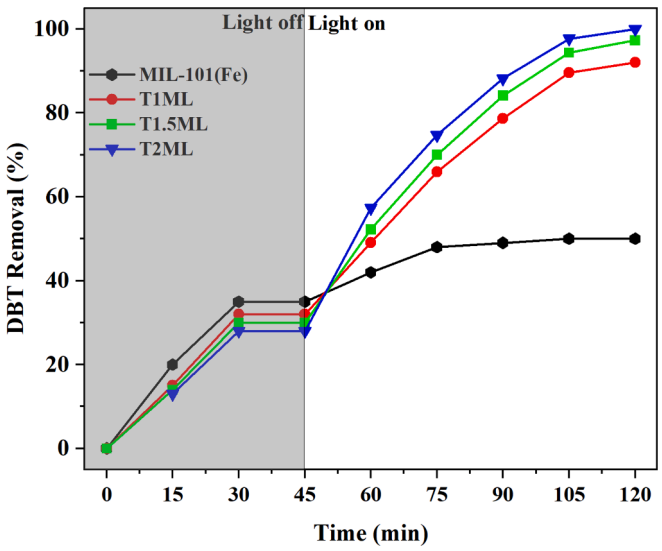

Fig. 14. Effect of synthesized samples on reaction efficiency and selection of optimal photocatalyst. (T = 40 ℃, O/S = 8, T2ML dose = 2 g/L, and S/F = 1).

(a), all samples loaded with titanium exhibit a higher level of photocurrent than pure MIL-101(Fe). This suggests the formation of a heterojunction following the loading of titanium, which enhances the interfacial charge transfer of MIL-101(Fe) [48]. In the synthesized samples, T2ML exhibited the highest photocurrent density, indicating that, according to the photophysical properties of this sample, it exhibited the best performance in the separation of photogenerated electrons and holes [49]. The results indicate that the photocurrent density remains constant over time, suggesting that the synthesized samples can continuously supply electrons and holes for the photocatalytic reaction [50]. In order to investigate the separation and transfer of the photogenerated electron pair and holes, the Nyquist diagrams obtained from EIS analysis were utilized [51]. These diagrams are presented in Fig. 13(b). The results of the EIS radius indicate that T2ML exhibits a higher speed of electron and hole pair transfer than other samples [52]. The reduction of the EIS radius indicates that the loading of titanium facilitates the separation of electrons and holes and improves the photocatalytic activity. This improvement can be attributed to heterogeneous binding between titanium species and MIL-101 (Fe), as well as more efficient charge interfacial properties [53]. The results indicate that T2ML exhibits the most favorable optical properties and has a notable capacity to generate stable •OH and $\bullet O_2^-$ radicals.

3.2. PODS optimization

The synthesized materials were evaluated to identify the optimal sample for the photocatalytic oxidation reaction, as illustrated in Fig. 14. Following 45 min of adsorption in a dark environment, no discernible change was observed in the remaining DBT concentration. Consequently, the photocatalytic oxidation process commenced. The T2ML sample demonstrated superior performance, with nearly complete removal of DBT within 120 min.

The initial concentration of organosulfur compounds during the desulfurization process represents a critical element in the control and enhancement of reaction efficiency. As shown in Fig. 15(a), as the initial concentration of DBT increased, its conversion rate is decreased, as reported in prior literature [54–56]. To achieve maximum removal of sulfur compounds and increase reaction yield using T2ML, the research aimed for a concentration of 250 ppm.

One important factor in achieving the maximum sulfur compound conversion rate and reaction efficiency is the catalyst dosage. The presence of a sufficient number of active sites on the catalyst in the reaction solution leads to increased absorption of sulfur compounds and generation of photogenerated charge carriers for conducting the photocatalytic oxidation reaction. An excessive increase in catalyst mass results in the formation of catalyst aggregates, which could impede light passage, and diminish production of photogenerated charge carriers, subsequently reducing reaction efficiency [3]. The influence of catalyst quantity on reaction efficiency was evaluated, as represented in Fig. 15 (b). As it is observable, a concentration of 1.5 g/L yields an ample quantity of active sites. If the catalyst was not used, the removal rate was 13 %, which is associated with the adsorption mechanism.

The removal of different organosulfur compounds during the PODS reaction is significantly influenced by the reaction temperature, resulting in a modification of the reaction efficiency. The optimization of the reaction temperature for the removal of DBT is depicted in Fig. 16(a). Fig. 16(a) illustrates that as the temperature rises to 50 ℃, there is a notable enhancement in the DBT removal due to the accelerated formation of active metal peroxides at elevated temperatures [57]. Beyond this temperature, the conversion rate of DBT and the reaction efficiency decrease. This is caused by the decomposition of H_2O_2 [58] and the creation of water in the reaction mixture.

The biphasic state of the PODS reaction solution and the carry of the converted organosulfur compounds (products) to the other phase have a

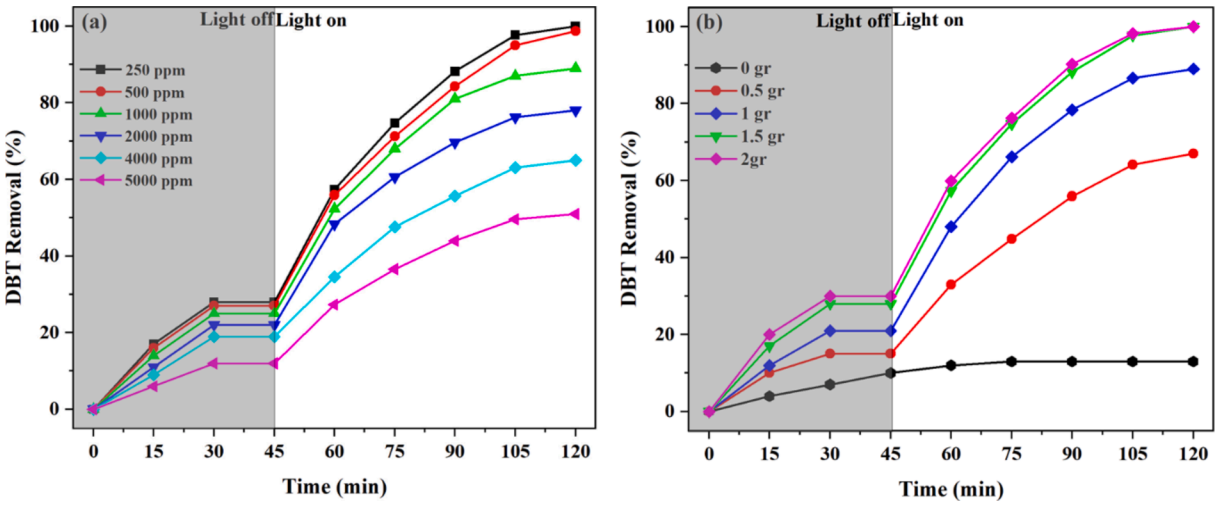

Fig. 15. Impact of (a) DBT concentration, (b) photocatalyst loading on the organosulfur removal. (T = 40 ℃, O/S = 8, T2ML dose = 2 g/L, and S/F = 1).

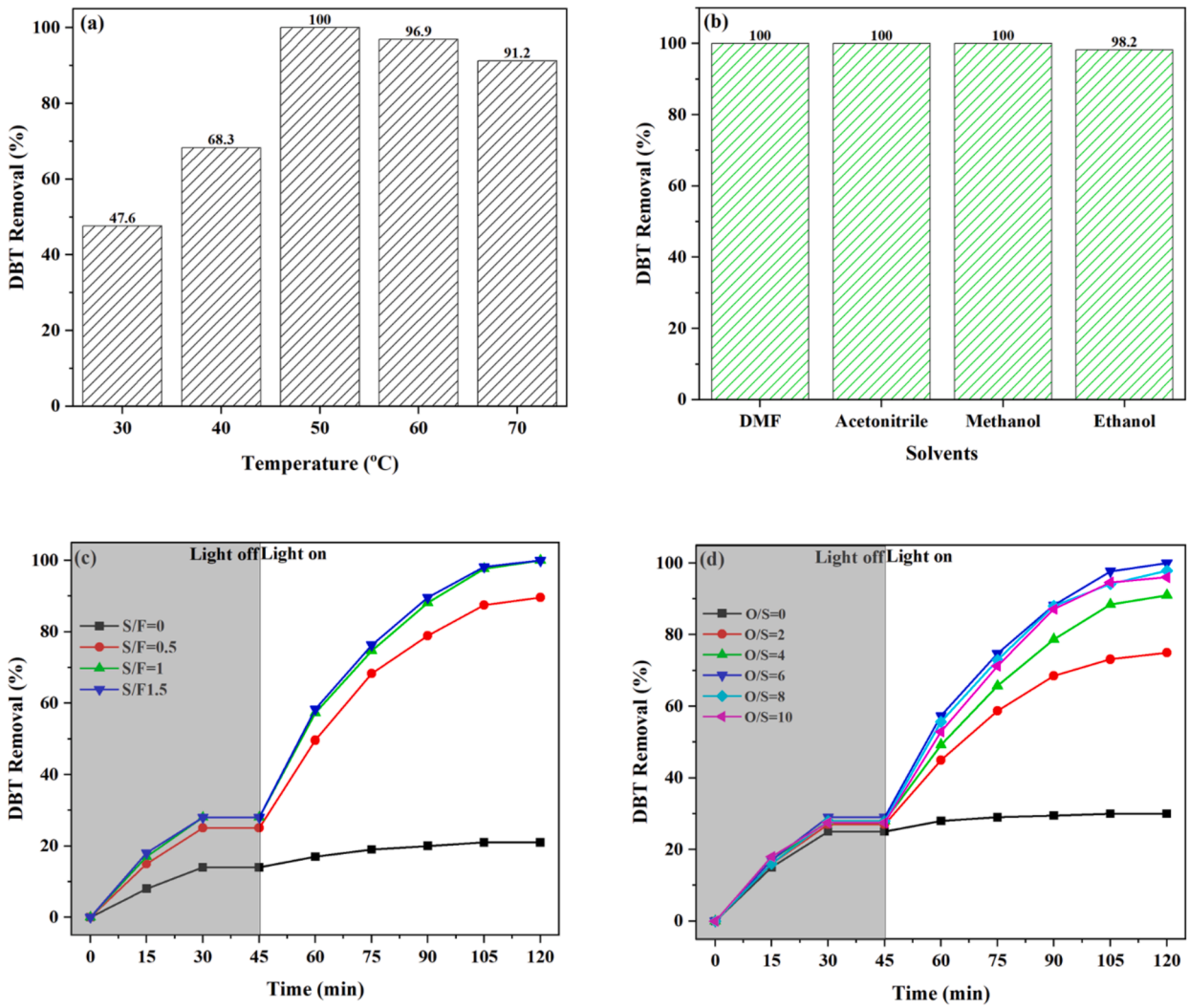

Fig. 16. Investigating the effect of (a) reactor temperature, (b) solvent kind, (c) S/F ratio, and (d) O/S on the DBT removal. (T = 50 ℃, O/S = 6, T2ML dose = 1.5 g/L and S/F = 1).

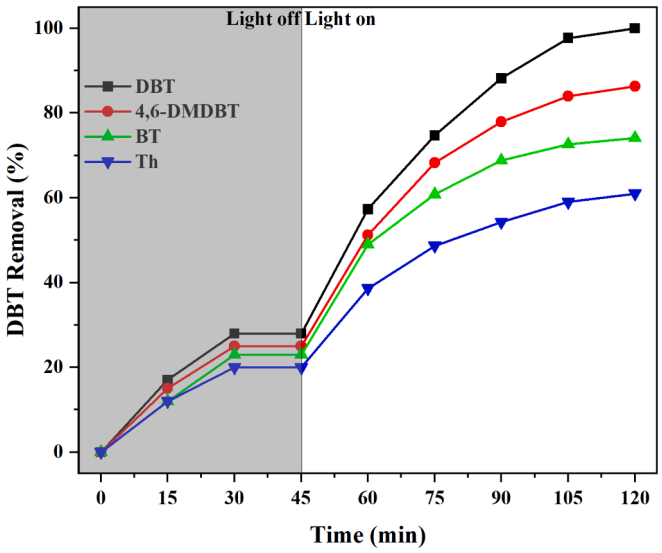

Fig. 17. Removal of various sulfur compounds over reaction time by T2ML photocatalyst. (T = 50 ℃, O/S = 6, T2ML dose = 1.5 g/L, and S/F = 1).

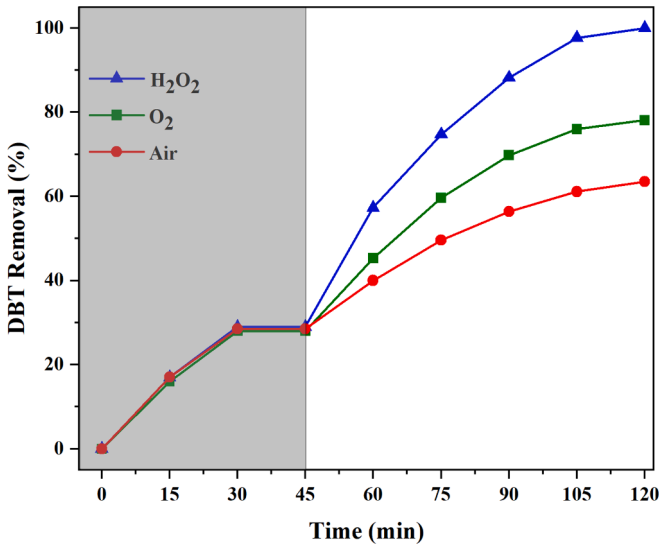

Fig. 18. The effect of different oxidants and oxidant phases on sulfur removal under optimal condition(T = 50 ℃, T2ML dose = 1.5 g/L, O/S = 6, and S/F = 1).

Table 2
A comparative analysis of the efficacy of various samples in the PODS reaction.

Catalyst	DBT Initial Concentration (ppm)	Oxidant	O/S ratio	Reaction time(min)	DBT removal (%)	Ref.
5 wt% MoO_3-TMU-5	521	Air	150 ml.min^{-1}	60	95.6	[23]
$BiVO_4$@HKUST-1	100	H_2O_2	14:1	60	95	[70]
ZIF-67@$CoWO_4$	100	H_2O_2	8:1	120	96.7	[71]
TiO_2/g-C_3N_4	500	H_2O_2	6:1	120	98.9	[72]
CeO_2/MIL-101(Fe)	500	H_2O_2	4:1	120	90	[73]
CdS@NH_2-MIL-125	100	O_2	–	1440	76.8	[74]
CuO-Fe_3O_4	250	H_2O_2	7.5:1	120	95	[75]
T1ML	250	H_2O_2	6:1	120	92	This work
T1.5ML	250	H_2O_2	6:1	120	97.3	This work
T2ML	250	H_2O_2	6:1	120	100	This work

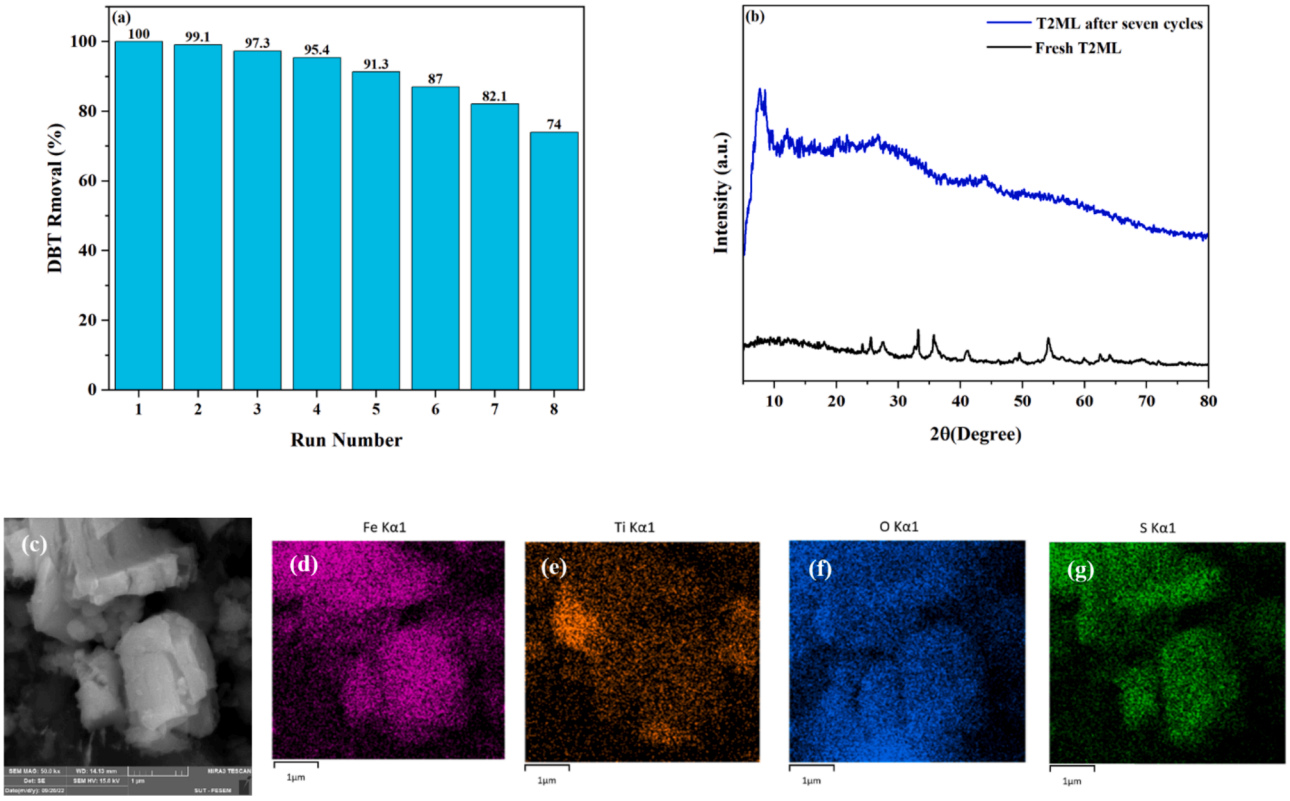

Fig. 19. (a) Recyclability (b) pattern of XRD and (c) EDX mapping and FESEM of T2ML after recyclability tests (T = 50 ℃, T2ML dose = 1.5 g/L, O/S = 6, and S/F = 1).

significant impact on the efficiency of the process, as shown in Fig. 16 (b). The selection of an appropriate solvent is therefore crucial. In general, selecting the appropriate solvent is determined by polarity [59] and its economic feasibility [60]. The results presented in Fig. 16(b) indicate that all three solvents, namely acetonitrile, methanol, and DMF, exhibited comparable performance levels. Nevertheless, methanol was selected as the preferred solvent due to its high availability and reasonable cost compared to the other options. The solvent volume has a considerable impact on the conversion of DBT in the PODS system solution. However, excessive solvent usage may directly impact the extraction process and result in errors during the PODS reaction. Fig. 16 (c) indicates that the highest level of DBT conversion (100 %) is achieved at a solvent to fuel volume ratio (S/F) of 1:1. Upon increasing the ratio to 1.5, no change was observed in the DBT removal rate. Consequently, S/F = 1 represents the optimal value.

The O/S ratio and bubble flow rate parameters significantly enhance the organosulfur conversion when utilizing liquid (H_2O_2) and gas (oxygen) oxidants in the PODS reaction [61,62]. The optimized O/S ratio results are presented in Fig. 16(d). It is obvious that increasing the ratio from 0 to 6 significantly increases the conversion of DBT due to the enhanced oxidation rate of DBT [63]. However, a further increase in this ratio results in a decrease in the conversion rate of DBT attributed to the decomposition of H_2O_2 [64] and the production of water in the reaction solution.

3.3. *The efficacy of T2ML in the removal of a variety of organosulfur compounds*

It is well established that real fuel contains a variety of sulfur compounds, as previously discussed. To assess T2ML's ability to remove these compounds, its performance was evaluated and the results are presented in Fig. 17. The order of sulfur compound removal was DBT > 4,6-DMDBT > BT > Th, which is well aligned with the results of previous literature [65]. The Th, DBT, BT, and 4,6- DMDBT had removal rates of 61 %, 100 %, 74.1 %, and 86.36 %, respectively. The oxidation rate of the various organosulfur compounds depends on the steric hindrance and electron density present on the sulfur atom [24]. The greater the electron density of the sulfur atom, the higher the oxidation level,

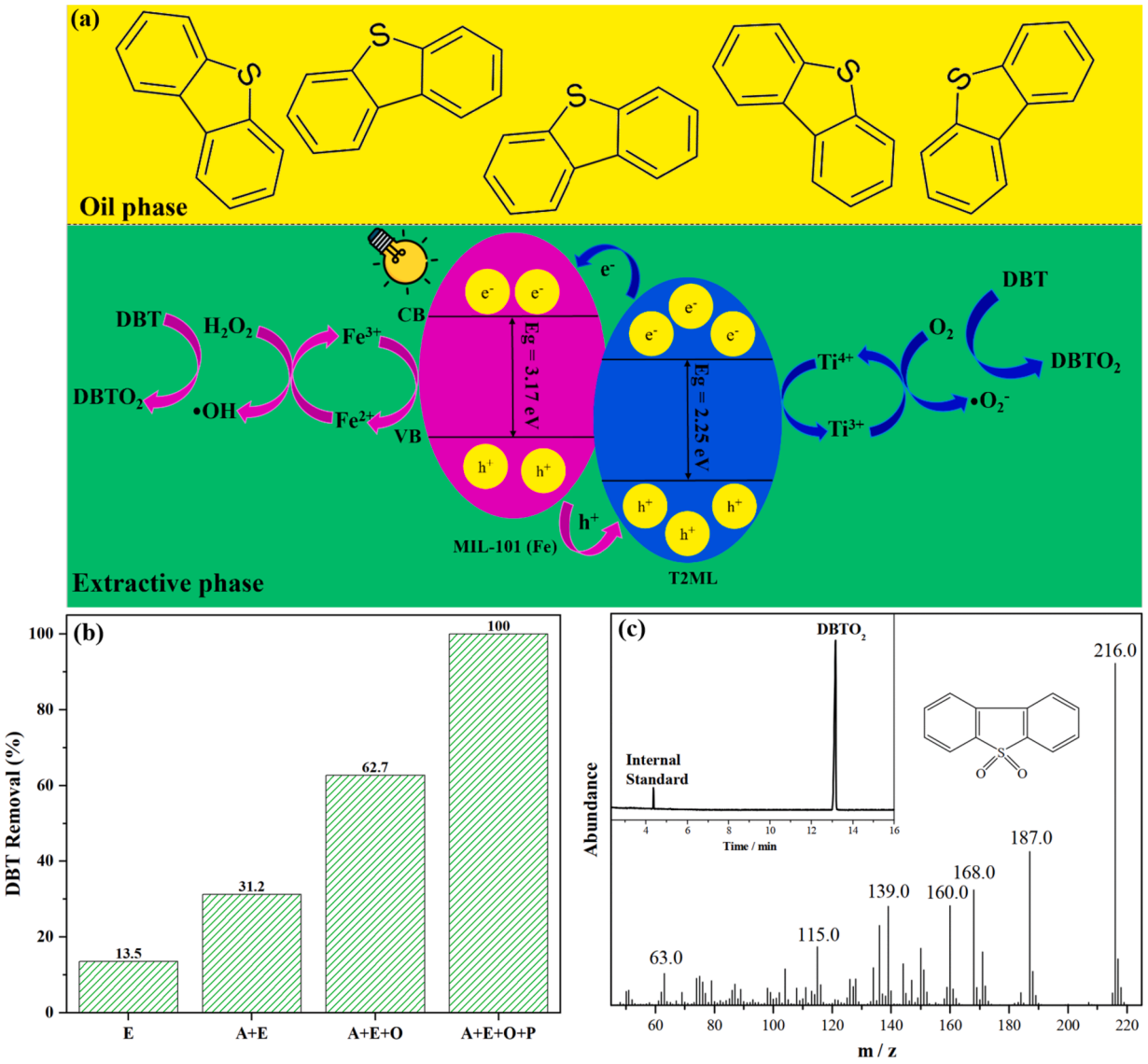

Fig. 20. Proposed mechanism (a) for the removal of DBT by T2ML, the extent of DBT removal by each mechanism/reaction (E/A/O/P) (b) (T = 50 ℃, T2ML dose = 1.5 g/L, O/S = 6, and S/F = 1), and GC–MS analysis (c) of extractive phase at the end of process.

resulting in an increased rate of removal. The electron densities of the sulfur atoms in Th, DBT, 4,6-DMDBT, and BT structures are 5.6, 5.758, 5.7, and 5.739, respectively [66]. The electron densities of the sulfur atoms in DBT, 4,6-DMDBT, and BT closely resemble each other. However, their removal rates differ significantly under the same conditions. This discrepancy is connected to the steric hindrance imposed by the methyl group, which results in a diminished reactivity of 4,6-DMDBT and BT in comparison to DBT.

3.4. The effect of different oxidants and oxidant phases on sulfur removal

Oxidants are employed in various industrial applications in the forms of solids, liquids, or gases [67]. In the PODS reaction, the nature of the reaction and the necessity of conducting it continuously have led researchers to focus their attention on the use of gaseous oxidants, such as air and oxygen. In this study, a flow rate of 100 ml/min has been employed for air and oxygen, a value that has been demonstrated to be optimal in a number of previous studies [68]. An excessive increase in the flow rate of the oxidant leads to a reduction in the efficacy of the photocatalyst. This phenomenon was attributed to the adhesion of sulfur compound molecules to the surface of the photocatalyst, resulting in a decrease in the light transmission rate [69]. The amount of DBT removal under optimal conditions by air and oxygen was 63.5 % and 78 %, respectively, as illustrated in Fig. 18. The most significant challenge associated with the utilization of gas oxidants in the PODS reaction is the reduction in reaction efficiency relative to conditions where hydrogen peroxide is employed. This discrepancy can be attributed to two primary factors: mass transfer resistance and the inability to generate •OH and $•O_2^-$ radicals to the same extent as hydrogen peroxide.

In Table 2, a comparison is presented between the performance and reaction conditions of different photocatalysts based on MOFs.

3.5. Catalyst recyclability

One crucial parameter for the industrial implementation of catalysts is their recyclability and stability [76]. To assess the catalyst's recyclability, the catalyst was separated by centrifugation (4000 rpm for 10 min) and washed with ethanol three times after each cycle. It was then dried at 90 °C for 12 h to prepare for the subsequent run under the previously determined optimal conditions. As shown in Fig. 19(a), the catalyst showed noteworthy stability for up to seven cycles, with a mere 20 % decline in activity. Upon comparing the XRD patterns of fresh and

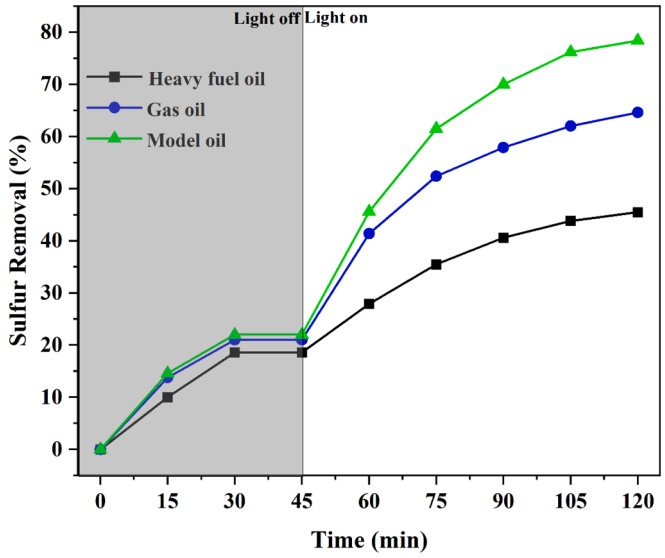

Fig. 21. Sulfur compounds removal from real fuel by T2ML under optimal condition (T = 50 ℃, T2ML dose = 1.5 g/L, O/S = 6, and S/F = 1).

utilized T2ML after repeated cycles (see Fig. 19(b)), it is evident that the crystal structure of T2ML has been annihilated, resulting in several alterations in the XRD pattern. The FESEM image and mapping of T2ML after seven cycles are depicted in Fig. 19(c), confirming the structural alteration and the existence of sulfur.

3.6. Possible PODS mechanism over T2ML photocatalyst

The mechanism proposed for eliminating DBT by T2ML is illustrated in Fig. 20 (a). By enhancing the oxidation rate through the oxidant, trapping electrons and h + in the conduction and valence bands, the PODS reaction generates $\bullet O_2^-$ and •OH. The PODS reaction product (sulfone) is formed by the reaction of DBT (organosulfur compounds) with •OH and $\bullet O_2^-$. The intermediates produced, namely Fe^{2+} and Ti^{3+}, result in the generation of •OH and $\bullet O_2^-$. Finally, the reaction of DBT and •OH/$\bullet O_2^-$ results in the production of the reaction product ($DBTO_2$). Previous observations [2,5] and the yellow color of the polar phase indicate that the reaction product is only $DBTO_2$. The following equations can describe the removal process:

$$T2ML + hv \rightarrow e^- + h^+ \quad (3)$$

$$Ti^{4+} + e^- \rightarrow Ti^{3+} \quad (4)$$

$$Ti^{3+} + H_2O_2 \rightarrow Ti^{4+} + \bullet OH + OH^- \quad (5)$$

$$H_2O_2 + \bullet OH \rightarrow H_2O + H^+ + \bullet O_2^- \quad (6)$$

$$2H_2O + 4h^+ \rightarrow O_2 + 4H^+ \quad (7)$$

$$Fe^{3+} + e^- \rightarrow Fe^{2+} \quad (8)$$

$$Fe^{2+} + O_2 \rightarrow Fe^{3+} + \bullet O_2^- \quad (9)$$

$$DBT + \bullet OH(\bullet O_2^-) \rightarrow DBTO_2 \quad (10)$$

The following equations [77] were employed to approximate the values of CB and VB for T2ML.

$$E_{VB} = X + 0.5E_g - E_e \quad (11)$$

$$E_{CB} = E_{VB} - E_g \quad (12)$$

where X is the electronegativity of semiconductor, E_e is the energy of free electrons (4.5 eV), and E_g represents the distance between the conduction band and the valence band, which is commonly referred to as the bandgap. The bandgap value for T2ML was determined to be 4 eV through the use of the UV–Vis DRS analysis. The calculation of X is based on the following equation:

$$X = \left[X(A)^a X(B)^b\right]^{\frac{1}{a+b}} \quad (13)$$

Table 3
Reaction rate constant, R-square, and kinetic rate equations, of PODS reaction at different temperature for T2ML.

Temperature (°C)	R-square	Kinetic equation	Reaction rate constant (min^{-1})
30	0.986	$0.00541x + 0.03045$	0.00541
40	0.98	$0.0099x - 0.03783$	0.0099
50	0.96	$0.02589x - 0.44624$	0.0259
60	0.91	$0.02912x - 0.45976$	0.02912
70	0.94	$0.04779x - 1.09913$	0.04779

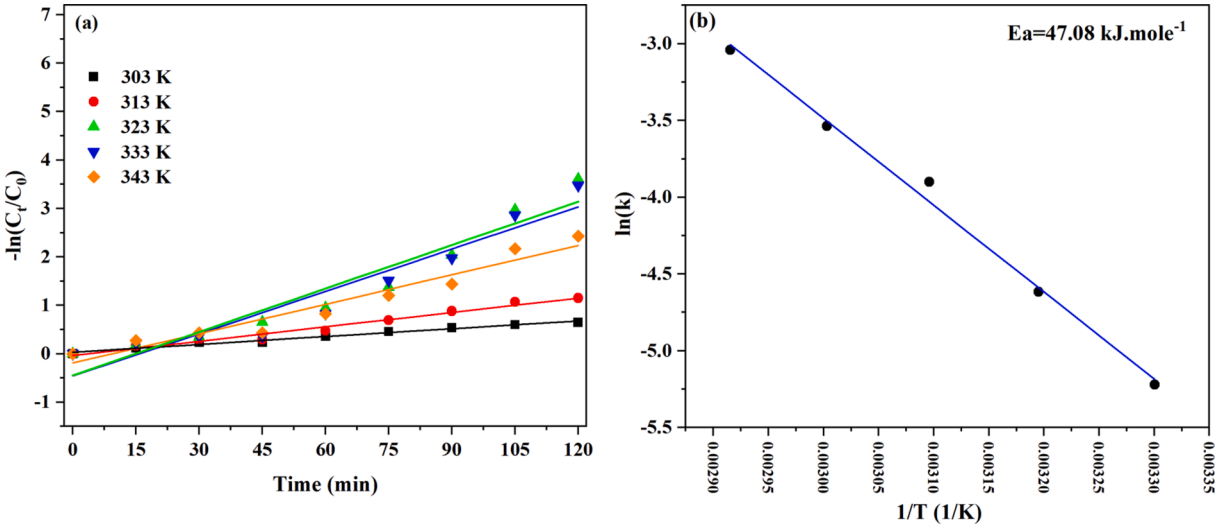

Fig. 22. DBT Removal at different temperature (Kinetics study): (a) Determination of the K (min^{-1}), (b) Ea ($Kj.mole^{-1}$).

where a and b and are the atomic number of compounds. The value of the *X* parameter for T2ML was approximately 5.51 eV. Therefore, VB and CB are equal to 2.135 eV and −0.115 eV for T2ML.

The PODS reaction is the result of the occurrence of four distinct chemical, physical, physicochemical, and light-dependent reactions simultaneously: extraction (E), adsorption (A), oxidation (O), and photocatalytic (P). In order to ascertain the efficacy of the photocatalytic reaction and the formation of •OH and $\bullet O_2^-$ radicals, the impact of each of the aforementioned sections was evaluated independently, with the performance of blank tests (Fig. 20 (b)). The results indicated that extraction, adsorption, oxidation, and radiation each accounted for 13.15 %, 17.7 %, 31.5 %, and 37.3 % of PODS action, respectively.

In order to verify the formation of the desired products and to confirm that the proposed mechanism for $DBTO_2$ formation was indeed operational, a GC–MS analysis was conducted, as illustrated in Fig. 20 (c). As illustrated in Fig. 20(c), no discernible peak corresponding to DBT was observed in the extracted phase. Conversely, a distinct peak at $m/z = 216$ [78] was identified, which corroborates the veracity of the PODS reaction and the proposed mechanism.

3.7. Sulfur compounds removal from real fuel

In order to assess the efficacy of T2ML in the simultaneous removal of diverse S-compounds, the sulfur compound removal rate from the real fuel and the constructed model fuel (containing 250 ppm Th, 250 ppm 4,6-DMDBT, 250 ppm BT, and 250 ppm DBT) was evaluated. The results are presented in Fig. 21. The T2ML photocatalyst was found to be effective in the removal of sulfur compounds from heavy fuel oil, gas oil, and model fuel, with a removal efficiency of 45.5 %, 64.6 %, and 78.4 %, respectively. These results are in good agreement with those reported in previous studies [79], indicating that T2ML can be a suitable option for the removal of sulfur compounds in fuels with a high sulfur content and resistant compounds.

3.8. Kinetic study

Studying the kinetics of the PODS reaction is critical to understanding the DBT removal process. The effect of temperature on the PODS reaction was assessed at various degrees, and the interactive correlation was derived by fitting. According to Fig. 22(a), the elimination of DBT in PODS reaction shows a pseudo-first order kinetic. The reaction rate constant (k) is determined by using Eq. 13, in which C_0 and C_t are the initial concentration and concentration at time t, respectively and k is the rate constant of the reaction. For the PODS reaction, the activation energy (Ea) was determined using the Arrhenius theory (Eq. 14) [80] (Fig. 22(b)). The kinetic equations, k and R-square at each temperature for T2ML are listed in Table 3.

$$-\ln\left(\frac{c_t}{c_0}\right) = kt \tag{14}$$

$$\ln k = \ln A - \frac{E_a}{RT} \tag{15}$$

4. Conclusion

Titanium species was introduced to the structure of MIL-101(Fe) in this research, and TxML photocatalysts were synthesized using the one pot solvothermal method. The synthesized photocatalysts were subjected to a series of characterization techniques, as detailed in the characterization section, to evaluate the physicochemical properties of the synthesized materials. Under visible light irradiation and optimal conditions (temperature = 50 ℃, oxidant to sulfur molar ratio = 6, photocatalyst loading = 1.5 g/L, and solvent to fuel volume ratio = 1), T2ML exhibited superior performance and successfully eliminated 100 % of DBT. Kinetic studies have demonstrated that the DBT removal follows a pseudo-first-order kinetic model. The results indicate that T2ML can be a highly effective sample for sulfur removal via the PODS reaction.

CRediT authorship contribution statement

Mehdi Beshtar: Writing – original draft, Investigation, Methodology. **Afsanehsadat Larimi:** Writing – review & editing, Supervision, Conceptualization, Funding acquisition, Project administration. **Ali Akbar Asgharinezhad:** Writing – review & editing, Supervision, Conceptualization, Resources.

Declaration of competing interest

The authors declare that they have no known competing financial interests or personal relationships that could have appeared to influence the work reported in this paper.

Data availability

Data will be made available on request.

Acknowledgment

The authors would like to express their sincere gratitude to Dr. Zahra Jafari for her invaluable guidance and insightful contributions throughout the development of this article.

References

[1] V. Chandra Srivastava, An evaluation of desulfurization technologies for sulfur removal from liquid fuels, RSC Adv. 2 (2012) 759–783, https://doi.org/10.1039/C1RA00309G.
[2] M. Beshtar, F. Khorasheh, A. Larimi, A. Akbar Asgharinezhad, Photocatalytic oxidative desulfurization of model fuel using iron-molybdenum nanocatalyst based on cerium oxide (FeyMox/CeO2) under visible light, Fuel 360 (2024) 130549, https://doi.org/10.1016/j.fuel.2023.130549.
[3] X. Zhou, T. Wang, H. Liu, X. Gao, C. Wang, G. Wang, Desulfurization through Photocatalytic Oxidation: A Critical Review, ChemSusChem 14 (2021) 492–511, https://doi.org/10.1002/cssc.202002144.
[4] A. Ostovar, A. Larimi, Z. Jiang, M. Lotfi, C. Ghotbi, F. Khorasheh, Enhanced visible-light photocatalytic oxidative desulfurization of model fuel over Pt-decorated carbon-doped TiO2 nanoparticles, Environ. Sci. Pollut. Res. (2023), https://doi.org/10.1007/s11356-023-26597-y.
[5] M. Beshtar, A. Akbar Asgharinezhad, A. Larimi, Ultra-deep photocatalytic oxidative desulfurization of liquid fuels by Ti@CeO2/ZnO nanophotocatalyst under visible light and mild operating conditions, J. Ind. Eng. Chem. (2024), https://doi.org/10.1016/j.jiec.2024.01.017.
[6] I. Shafiq, S. Shafique, P. Akhter, G. Abbas, A. Qurashi, M. Hussain, Efficient catalyst development for deep aerobic photocatalytic oxidative desulfurization: recent advances, confines, and outlooks, Catal. Rev. Sci. Eng. (2021), https://doi.org/10.1080/01614940.2020.1864859.
[7] X. Li, Z. Zhang, C. Yao, X. Lu, X. Zhao, C. Ni, Attapulgite-CeO2/MoS2 ternary nanocomposite for photocatalytic oxidative desulfurization, Appl. Surf. Sci. 364 (2016) 589–596, https://doi.org/10.1016/j.apsusc.2015.12.196.
[8] J. Qiu, X. Zhang, Y. Feng, X. Zhang, H. Wang, J. Yao, Modified metal-organic frameworks as photocatalysts, Appl. Catal. B 231 (2018) 317–342, https://doi.org/10.1016/j.apcatb.2018.03.039.
[9] C.-C. Wang, J.-R. Li, X.-L. Lv, Y.-Q. Zhang, G. Guo, Photocatalytic organic pollutants degradation in metal–organic frameworks, Energy Environ. Sci. 7 (2014) 2831–2867, https://doi.org/10.1039/C4EE01299B.
[10] Y. Zhang, G. Li, L. Kong, H. Lu, Deep oxidative desulfurization catalyzed by Ti-based metal-organic frameworks, Fuel 219 (2018) 103–110, https://doi.org/10.1016/j.fuel.2018.01.050.
[11] H.D. Lawson, S.P. Walton, C. Chan, Metal-organic frameworks for drug delivery: a design perspective, ACS Appl. Mater Interfaces 13 (2021) 7004–7020, https://doi.org/10.1021/acsami.1c01089.
[12] M.T. Kapelewski, T. Runčevski, J.D. Tarver, H.Z.H. Jiang, K.E. Hurst, P.A. Parilla, A. Ayala, T. Gennett, S.A. FitzGerald, C.M. Brown, J.R. Long, Record High Hydrogen Storage Capacity in the Metal-Organic Framework Ni2(m-dobdc) at Near-Ambient Temperatures, Chem. Mater. 30 (2018) 8179–8189, https://doi.org/10.1021/acs.chemmater.8b03276.
[13] W. Li, Metal–organic framework membranes: Production, modification, and applications, Prog Mater Sci 100 (2019) 21–63, https://doi.org/10.1016/j.pmatsci.2018.09.003.
[14] S. Gautam, H. Agrawal, M. Thakur, A. Akbari, H. Sharda, R. Kaur, M. Amini, Metal oxides and metal organic frameworks for the photocatalytic degradation: A review,

J Environ Chem Eng 8 (2020) 103726, https://doi.org/10.1016/j.jece.2020.103726.
[15] X. Zhao, Y. Wang, D.-S. Li, X. Bu, P. Feng, Metal-Organic Frameworks for Separation, Adv. Mater. 30 (2018) 1705189, https://doi.org/10.1002/adma.201705189.
[16] A. Kuznicki, G.R. Lorzing, E.D. Bloch, Tuning water adsorption, stability, and phase in Fe-MIL-101 and Fe-MIL-88 analogs with amide functionalization, Chem. Commun. 57 (2021) 8312–8315, https://doi.org/10.1039/D1CC02104D.
[17] A.A. Taha, L. Huang, S. Ramakrishna, Y. Liu, MOF [NH2-MIL-101(Fe)] as a powerful and reusable Fenton-like catalyst, J. Water Process Eng. 33 (2020) 101004, https://doi.org/10.1016/j.jwpe.2019.101004.
[18] S. Peng, R. Li, Y. Rao, Y. Huang, Y. Zhao, M. Xiong, J. Cao, S. Lee, Tuning the unsaturated iron sites in MIL-101(Fe) nanoparticles for reactive oxygen species-mediated bacterial inactivation in the dark, Appl Catal B 316 (2022) 121693, https://doi.org/10.1016/j.apcatb.2022.121693.
[19] M.Y. Zorainy, M. Gar Alalm, S. Kaliaguine, D.C. Boffito, Revisiting the MIL-101 metal–organic framework: design, synthesis, modifications, advances, and recent applications, J Mater Chem A Mater 9 (2021) 22159–22217, https://doi.org/10.1039/D1TA06238G.
[20] S.-W. Li, W. Wang, J.-S. Zhao, Highly effective oxidative desulfurization with magnetic MOF supported W-MoO3 catalyst under oxygen as oxidant, Appl Catal B 277 (2020) 119224, https://doi.org/10.1016/j.apcatb.2020.119224.
[21] S. Hamzehzad, M. Feyzi, L. norouzi, Synthesis of GO/Fe–Ni MOF octahedral structure as an effective magnetic adsorbent in the removal of sulfur compounds from liquid fuel, Mater Sci Semicond Process 156 (2023) 107296. https://doi.org/https://doi.org/10.1016/j.mssp.2022.107296.
[22] A. Haruna, Z.M.A. Merican, S.G. Musa, Remarkable stability and catalytic performance of PW11M@MOF-808 (M=Mn and Cu) nanocomposites for oxidative desulfurization of fuel oil, Mol. Catal. 541 (2023) 113079, https://doi.org/10.1016/j.mcat.2023.113079.
[23] M. Bagheri, M.Y. Masoomi, A. Morsali, A MoO3–Metal–Organic Framework Composite as a Simultaneous Photocatalyst and Catalyst in the PODS Process of Light Oil, ACS Catal 7 (2017) 6949–6956, https://doi.org/10.1021/acscatal.7b02581.
[24] K. Zhang, F. Chu, Y. Hu, X. Huang, G. Zhao, G. Wang, Ce-doped MIL-125-NH2 coupled Ce4+/Ce3+ and Ti4+/Ti3+ redox mediators for thermo-enhanced photocatalytic oxidative desulfurization, Chin. Chem. Lett. 34 (2023) 107766, https://doi.org/10.1016/j.cclet.2022.107766.
[25] L. He, Y. Dong, Y. Zheng, Q. Jia, S. Shan, Y. Zhang, A novel magnetic MIL-101(Fe)/TiO2 composite for photo degradation of tetracycline under solar light, J Hazard Mater 361 (2019) 85–94, https://doi.org/10.1016/j.jhazmat.2018.08.079.
[26] M. Zarrabi, M.H. Entezari, Modification of C/TiO2@MCM-41 with nickel nanoparticles for photocatalytic desulfurization enhancement of a diesel fuel model under visible light, J Colloid Interface Sci 457 (2015) 353–359, https://doi.org/10.1016/j.jcis.2015.07.021.
[27] C. Zhao, P. Dong, Z. Liu, G. Wu, S. Wang, Y. Wang, F. Liu, Facile synthesis of Fe3O4/MIL-101 nanocomposite as an efficient heterogeneous catalyst for degradation of pollutants in Fenton-like system, RSC Adv 7 (2017) 24453–24461, https://doi.org/10.1039/c7ra01883e.
[28] X. Li, W. Guo, Z. Liu, R. Wang, H. Liu, Quinone-modified NH2-MIL-101(Fe) composite as a redox mediator for improved degradation of bisphenol A, J Hazard Mater 324 (2017) 665–672, https://doi.org/10.1016/j.jhazmat.2016.11.040.
[29] W. Zhu, Y. Xu, H. Li, B. Dai, H. Xu, C. Wang, Y. Chao, H. Liu, Photocatalytic oxidative desulfurization of dibenzothiophene catalyzed by amorphous TiO2 in ionic liquid, Korean J. Chem. Eng. 31 (2014) 211–217, https://doi.org/10.1007/s11814-013-0224-3.
[30] M. Abdollahi, A. Larimi, Z. Jiang, F. Khorasheh, C. Ghotbi, Photocatalytic oxidative desulfurization of model fuel over visible light-active Cu-impregnated carbon-doped TiO2, J Clean Prod 380 (2022) 134968, https://doi.org/10.1016/j.jclepro.2022.134968.
[31] G. Srinivas, W. Travis, J. Ford, H. Wu, Z.-X. Guo, T. Yildirim, Nanoconfined ammonia borane in a flexible metal–organic framework Fe–MIL-53: clean hydrogen release with fast kinetics, J Mater Chem A Mater 1 (2013) 4167–4172, https://doi.org/10.1039/C3TA00037K.
[32] X. Yue, W. Guo, X. Li, H. Zhou, R. Wang, Core-shell Fe3O4@MIL-101(Fe) composites as heterogeneous catalysts of persulfate activation for the removal of Acid Orange 7, Environ. Sci. Pollut. Res. 23 (2016) 15218–15226, https://doi.org/10.1007/s11356-016-6702-5.
[33] J. Liang, M. Fan, W. Wu, M. Wu, W. Cai, G. Xinxing, T. Huang, H. Rui, Encapsulation of Sandwich POM in MIL-101 as Efficient Oxidative Desulfurization Catalyst of DBT, Catal Letters 153 (2023) 1159–1169, https://doi.org/10.1007/s10562-022-04057-5.
[34] M. Beshtar, A. Larimi, A.A. Asgharinezhad, F. Khorasheh, Ultra-deep Photocatalytic Oxidative Desulfurization of Model Fuel Using Ti-UiO-66(Zr) Metal-Organic Framework, Catal Letters (2023), https://doi.org/10.1007/s10562-023-04506-9.
[35] M.-J. Duan, Z. Guan, Y.-W. Ma, J.-Q. Wan, Y. Wang, Y.-F. Qu, A novel catalyst of MIL-101(Fe) doped with Co and Cu as persulfate activator: synthesis, characterization, and catalytic performance, Chem. Pap. 72 (2018) 235–250, https://doi.org/10.1007/s11696-017-0276-7.
[36] X.J. Wang, F.T. Li, J.X. Liu, C.G. Kou, Y. Zhao, Y.J. Hao, D. Zhao, Preparation of TiO2 in ionic liquid via microwave radiation and in situ photocatalytic oxidative desulfurization of diesel oil, in, Energy Fuel (2012) 6777–6782, https://doi.org/10.1021/ef301337y.
[37] R.F. Shafi, S.H. Ammar, M.K. Rashed, Catalytic/photocatalytic oxidative desulfurization activities of heteropolyacid immobilized on magnetic polythiophene nanocatalyst, J. Sulfur Chem. 42 (2021) 443–463, https://doi.org/10.1080/17415993.2021.1906245.
[38] S. Salehian, A. Larimi, A.A. Asgharinezhad, N. Khallaghi, T.N. Borhani, C. Ghotbi, Magnetic Z-scheme bismuth molybdate(1–x)/Fe3O4@MIL-125(Ti)(x) nanocomposite as a high-performance visible-light-active photocatalyst for ultra-deep oxidative desulfurization of liquid fuel, Surf. Interfaces 42 (2023) 103432, https://doi.org/10.1016/j.surfin.2023.103432.
[39] Y. Zhen, J. Wang, F. Fu, W. Fu, Y. Liang, The novel z-scheme ternary-component ag/agi/α-moo3 catalyst with excellent visible-light photocatalytic oxidative desulfurization performance for model fuel, Nanomaterials 9 (2019), https://doi.org/10.3390/nano9071054.
[40] S. Li, N. Mominou, Z. Wang, L. Liu, L. Wang, Ultra-deep Desulfurization of Gasoline with CuW/TiO2–GO through Photocatalytic Oxidation, Energy Fuel 30 (2016) 962–967, https://doi.org/10.1021/acs.energyfuels.5b02790.
[41] X. Zhou, T. Wang, H. liu, L. Zhang, C. Zhang, N. Kong, D. Su, C. Wang, Design of S-scheme heterojunction catalyst based on structural defects for photocatalytic oxidative desulfurization application, J Photochem Photobiol A Chem 433 (2022) 114162. https://doi.org/https://doi.org/10.1016/j.jphotochem.2022.114162.
[42] S. Xie, X. Zhao, D. Wang, H. Yang, L. Yang, L. Bai, D. Wei, W. Wang, Y. Liang, H. Chen, S. Guo, MoOx nanoclusters on Mo-doped TiO2 nanosheets with enhanced singlet oxygen generation and sulfide conversion abilities for photocatalytic aerobic oxidative desulfurization, Sci China Chem 67 (2024) 408–414, https://doi.org/10.1007/s11426-023-1728-6.
[43] P. Jabbari, A. Najafi Chermahini, R. Luque, A. Pineda, E.-R. Castellón, Synthesis of Cu-doped TiO2 modified BiVO4 for photocatalytic oxidative desulfurization (PODS) of a model fuel, J Photochem Photobiol A Chem 452 (2024) 115625, https://doi.org/10.1016/j.jphotochem.2024.115625.
[44] C.N.C. Hitam, A.A. Jalil, S. Triwahyono, A.F.A. Rahman, N.S. Hassan, N. F. Khusnun, S.F. Jamian, C.R. Mamat, W. Nabgan, A. Ahmad, Effect of carbon-interaction on structure-photoactivity of Cu doped amorphous TiO2 catalysts for visible-light-oriented oxidative desulphurization of dibenzothiophene, Fuel 216 (2018) 407–417, https://doi.org/10.1016/j.fuel.2017.12.035.
[45] M.S. Radwan, W.A. Aboutaleb, A.M.A. El Naggar, H.A. El Sayed, M.R. Shehata, S. S. Medany, Photo-oxidative extractive desulfurization of dibenzothiofene over Fe2O3-CeO2 nanocomposites at visible light irradiation, J Photochem Photobiol A Chem 433 (2022) 114137, https://doi.org/10.1016/j.jphotochem.2022.114137.
[46] Z. Liu, W. He, Q. Zhang, H. Shapour, M.F. Bakhtari, Preparation of a GO/MIL-101 (Fe) Composite for the Removal of Methyl Orange from Aqueous Solution, ACS Omega 6 (2021) 4597–4608, https://doi.org/10.1021/acsomega.0c05091.
[47] Y. Han, M. Liu, K. Li, Y. Zuo, Y. Wei, S. Xu, G. Zhang, C. Song, Z. Zhang, X. Guo, Facile synthesis of morphology and size-controlled zirconium metal-organic framework UiO-66: the role of hydrofluoric acid in crystallization, CrstEngComm 17 (2015) 6434–6440, https://doi.org/10.1039/c5ce00729a.
[48] C. Hu, J. Yin, S. Xun, L. Zhu, H. Li, M. He, P. Wu, H. Li, W. Zhu, Constructing interface chemical coupling S-scheme heterojunction MoO3-x@PPy for enhancing photocatalytic oxidative desulfurization performance: Adjusting LSPR effect via oxygen vacancy engineering, Applied Catalysis b: Environment and Energy 355 (2024) 124155, https://doi.org/10.1016/j.apcatb.2024.124155.
[49] A.A. Ismail, S.M. Albukhari, L.A. Al-Hajji, Fabrication of BiVO4 nanosheets decorating by V2O5 nanoparticles for the enhanced photocatalytic desulfurization of thiophene, J Environ Chem Eng 11 (2023) 109429, https://doi.org/10.1016/j.jece.2023.109429.
[50] C.N.C. Hitam, A.A. Jalil, A.A. Abdulrasheed, A review on recent progression of photocatalytic desulphurization study over decorated photocatalysts, J. Ind. Eng. Chem. 74 (2019) 172–186, https://doi.org/10.1016/j.jiec.2019.02.024.
[51] X. Lu, X. Li, J. Qian, N. Miao, C. Yao, Z. Chen, Synthesis and characterization of CeO2/TiO2 nanotube arrays and enhanced photocatalytic oxidative desulfurization performance, J Alloys Compd 661 (2016) 363–371, https://doi.org/10.1016/j.jallcom.2015.11.148.
[52] H. Zhang, T. Su, S. Yu, W. Liao, W. Ren, Z. Zhu, K. Yang, C. Len, G. Dong, D. Zhao, H. Lü, Fabrication of Anderson-Polyoxometalates/TiO2/C3N4 heterojunction composite for efficient visible-light-driven photooxidative desulfurization, Mol. Catal. 536 (2023) 112916, https://doi.org/10.1016/j.mcat.2023.112916.
[53] H. Chang, H. Yi, J. Zhang, Preparation of a NiO-Bi2WO6 catalyst and its photocatalytic oxidative desulfurization performance, Colloid Interface Sci Commun 41 (2021) 100381, https://doi.org/10.1016/j.colcom.2021.100381.
[54] W. Zhang, X. Li, H. Wang, Y. Song, S. Zhang, C. Li, Deep desulfurization of model oil by photocatalytic air oxidation and adsorption using Ti(1–x)MxO2 (M=Zr, Ce), Korean J. Chem. Eng. 34 (2017) 3132–3141, https://doi.org/10.1007/s11814-017-0229-4.
[55] W. Zhu, C. Wang, H. Li, P. Wu, S. Xun, W. Jiang, Z. Chen, Z. Zhao, H. Li, One-pot extraction combined with metal-free photochemical aerobic oxidative desulfurization in deep eutectic solvent, Green Chem. 17 (2015) 2464–2472, https://doi.org/10.1039/C4GC02425G.
[56] X. Zeng, X. Xiao, Y. Li, J. Chen, H. Wang, Deep desulfurization of liquid fuels with molecular oxygen through graphene photocatalytic oxidation, Appl Catal B 209 (2017) 98–109, https://doi.org/10.1016/j.apcatb.2017.02.077.
[57] F. Boshagh, M. Rahmani, K. Rostami, M. Yousefifar, Key Factors Affecting the Development of Oxidative Desulfurization of Liquid Fuels: A Critical Review, Energy Fuel 36 (2022) 98–132, https://doi.org/10.1021/acs.energyfuels.1c03396.
[58] X. Li, X. Yang, F. Zhou, J. Zhang, H. Yang, Y. Wang, Y. Zhao, X. Yuan, J. Ju, S. Hu, Construction of novel amphiphilic [Bmin]3PMo12O40/g-C3N4 heterojunction catalyst with outstanding photocatalytic oxidative desulfurization performance under visible light, J. Taiwan Inst. Chem. Eng. 100 (2019) 210–219, https://doi.org/10.1016/j.jtice.2019.04.024.

[59] I. Shafiq, M. Hussain, S. Shafique, R. Rashid, P. Akhter, A. Ahmed, J.-K. Jeon, Y.-K. Park, Oxidative desulfurization of refinery diesel pool fractions using LaVO4 photocatalyst, J. Ind. Eng. Chem. 98 (2021) 283–288, https://doi.org/10.1016/j.jiec.2021.03.040.
[60] S. Lin, S.-F. Ng, W.-J. Ong, Life cycle assessment of environmental impacts associated with oxidative desulfurization of diesel fuels catalyzed by metal-free reduced graphene oxide, Environ. Pollut. 288 (2021) 117677, https://doi.org/10.1016/j.envpol.2021.117677.
[61] W. Zhang, H. Zhang, J. Xiao, Z. Zhao, M. Yu, Z. Li, Carbon nanotube catalysts for oxidative desulfurization of a model diesel fuel using molecular oxygen, Green Chem. 16 (2014) 211–220, https://doi.org/10.1039/C3GC41106K.
[62] X.-M. Gao, F. Fu, L.-P. Zhang, W.-H. Li, The preparation of Ag–BiVO4 metal composite oxides and its application in efficient photocatalytic oxidative thiophene, Physica B Condens Matter 419 (2013) 80–85, https://doi.org/10.1016/j.physb.2013.03.024.
[63] X. Zhou, H. Liu, S. Liu, L. zhang, T. Wang, C. Wang, D. Su, Constructing efficient α-Fe2O3/g-C3N4/HNTs-loaded heterojunction photocatalysts for photocatalytic oxidative desulfurization: Influencing factors, kinetics, and mechanism, Fuel 332 (2023) 126147. https://doi.org/https://doi.org/10.1016/j.fuel.2022.126147.
[64] G. Miao, D. Huang, X. Ren, X. Li, Z. Li, J. Xiao, Visible-light induced photocatalytic oxidative desulfurization using BiVO4/C3N4@SiO2 with air/cumene hydroperoxide under ambient conditions, Appl Catal B 192 (2016) 72–79, https://doi.org/10.1016/j.apcatb.2016.03.033.
[65] J. Cui, G. Wang, W. Liu, P. Ke, Q. Tian, X. Li, Y. Tian, Synthesis BiVO4 modified by CuO supported onto bentonite for molecular oxygen photocatalytic oxidative desulfurization of fuel under visible light, Fuel 290 (2021) 120066, https://doi.org/10.1016/j.fuel.2020.120066.
[66] S. Otsuki, T. Nonaka, N. Takashima, W. Qian, A. Ishihara, T. Imai, T. Kabe, Oxidative Desulfurization of Light Gas Oil and Vacuum Gas Oil by Oxidation and Solvent Extraction, Energy Fuel 14 (2000) 1232–1239, https://doi.org/10.1021/ef000096i.
[67] M. Zbuzant, Issue 1 Citation M. Zbuzant*, An Overview of the Use of Photo Catalysts for Desulfurization, 2022.
[68] R. Liu, J. Zhang, Z. Xu, D. Zhao, S. Sun, Visible light photocatalytic oxidative desulfurization using Ti-MCM-41-loaded iron phthalocyanine combined with ionic liquid extraction, J. Mater. Sci. 53 (2018) 4927–4938, https://doi.org/10.1007/s10853-017-1954-0.
[69] H.F. Mohd Zaid, F.K. Chong, M.I. Abdul Mutalib, Photooxidative–extractive deep desulfurization of diesel using Cu–Fe/TiO2 and eutectic ionic liquid, Fuel 156 (2015) 54–62, https://doi.org/10.1016/j.fuel.2015.04.023.
[70] A. Raeisi, A. Najafi Chermahini, M.M. Momeni, A novel photocatalytic and photoelectrocatalytic system for oxidative desulfurization of model fuel using BiVO4@HKUST-1 composite in powder and deposited on fluorine-doped tin oxide, J. Photochem. Photobiol. A Chem. 433 (2022) 114190, https://doi.org/10.1016/j.jphotochem.2022.114190.
[71] S.M. Flihh, S.H. Ammar, Zeolitic imidazolate framework grafted by cobalt tungstate as an efficient photocatalyst for photocatalytic oxidative desulfurization of dibenzothiophene, Mater. Sci. Semicond. Process. 149 (2022) 106894, https://doi.org/10.1016/j.mssp.2022.106894.
[72] C. Wang, W. Zhu, Y. Xu, H. Xu, M. Zhang, Y. Chao, S. Yin, H. Li, J. Wang, Preparation of TiO2/g-C3N4 composites and their application in photocatalytic oxidative desulfurization, Ceram. Int. 40 (2014) 11627–11635, https://doi.org/10.1016/j.ceramint.2014.03.156.
[73] Q. Huo, G. Liu, H. Sun, Y. Fu, Y. Ning, B. Zhang, X. Zhang, J. Gao, J. Miao, X. Zhang, S. Liu, CeO2-modified MIL-101(Fe) for photocatalysis extraction oxidation desulfurization of model oil under visible light irradiation, Chem. Eng. J. 422 (2021), https://doi.org/10.1016/J.CEJ.2021.130036.
[74] M. Hosseini-Sarvari, S. Saki, Y. Gu, D. Zheng, In situ synthesis of CdS@NH2-MIL-125 nanocomposite for the enhanced photocatalytic oxidative desulfurization of dibenzothiophene, Catal. Sci. Technol. 13 (2023) 874–886, https://doi.org/10.1039/D2CY01837C.
[75] S.H. Ammar, Y.S. Kareem, A.D. Ali, Photocatalytic oxidative desulfurization of liquid petroleum fuels using magnetic CuO–Fe3O4 nanocomposites, J. Environ. Chem. Eng. 6 (2018) 6780–6786, https://doi.org/10.1016/j.jece.2018.10.031.
[76] Y. Lu, C. Yue, B. Liu, M. Zhang, Y. Li, W. Yang, Y. Lin, Y. Pan, D. Sun, Y. Liu, The encapsulation of POM clusters into MIL-101(Cr) at molecular level: LaW10O36@MIL-101(Cr), an efficient catalyst for oxidative desulfurization, Microporous Mesoporous Mater. 311 (2021) 110694, https://doi.org/10.1016/j.micromeso.2020.110694.
[77] X. Yang, W. Gu, Y. Ma, S. Zhai, F. Teng, Interface electron transfer of Bi2MoO6/MIL-125 and the visible-light performance for pollutant degradation, Colloids Surf A Physicochem. Eng. Asp. 597 (2020) 124748, https://doi.org/10.1016/j.colsurfa.2020.124748.
[78] S. Xun, W. Zhu, Y. Chang, H. Li, M. Zhang, W. Jiang, D. Zheng, Y. Qin, H. Li, Synthesis of supported SiW12O40-based ionic liquid catalyst induced solvent-free oxidative deep-desulfurization of fuels, Chem. Eng. J. 288 (2016) 608–617, https://doi.org/10.1016/j.cej.2015.12.005.
[79] M.A. Rezvani, S. Hosseini, H. Hassani Ardeshiri, Highly Efficient Catalytic Oxidative Desulfurization of Gasoline Using PMnW11@PANI@CS as a New Inorganic-Organic Hybrid Nanocatalyst, Energy Fuel 36 (2022) 7722–7732, https://doi.org/10.1021/acs.energyfuels.2c00997.
[80] S. Subhan, M. Yaseen, B. Ahmad, Z. Tong, F. Subhan, W. Ahmad, M. Sahibzada, Fabrication of MnO2NPs incorporated UiO-66 for the green and efficient oxidative desulfurization and denitrogenation of fuel oils, J. Environ. Chem. Eng. 9 (2021), https://doi.org/10.1016/j.jece.2021.105179.